NEARLY EXACT AND HIGHLY EFFICIENT ELASTIC-PLASTIC
HOMOGENIZATION AND/OR DIRECT NUMERICAL SIMULATION OF
LOW-MASS METALLIC SYSTEMS WITH
ARCHITECTED CELLULAR MICROSTRUCTURES

Maryam Tabatabaei, Dy Le and Satya N. Atluri

msp

NEARLY EXACT AND HIGHLY EFFICIENT ELASTIC-PLASTIC HOMOGENIZATION AND/OR DIRECT NUMERICAL SIMULATION OF LOW-MASS METALLIC SYSTEMS WITH ARCHITECTED CELLULAR MICROSTRUCTURES

MARYAM TABATABAEI, DY LE AND SATYA N. ATLURI

Additive manufacturing has enabled the fabrication of lightweight materials with intricate cellular architectures. These materials are interesting due to their properties which can be optimized upon the choice of the parent material and the topology of the architecture, making them appropriate for a wide range of applications including lightweight aerospace structures, energy absorption, thermal management, metamaterials, and bioscaffolds. In this paper we present the simplest initial computational framework for the analysis, design, and topology optimization of low-mass metallic systems with architected cellular microstructures. A very efficient elastic-plastic homogenization of a repetitive Representative Volume Element (RVE) of the microlattice is proposed. Each member of the cellular microstructure undergoing large elastic-plastic deformations is modeled using only one nonlinear three-dimensional (3D) beam element with 6 degrees of freedom (DOF) at each of the 2 nodes of the beam. The nonlinear coupling of axial, torsional, and bidirectional-bending deformations is considered for each 3D spatial beam element. The plastic hinge method, with arbitrary locations of the hinges along the beam, is utilized to study the effect of plasticity. We derive an explicit expression for the tangent stiffness matrix of each member of the cellular microstructure using a mixed variational principle in the updated Lagrangian corotational reference frame. To solve the incremental tangent stiffness equations, a newly proposed Newton homotopy method is employed. In contrast to the Newton's method and the Newton–Raphson iteration method, which require the inversion of the Jacobian matrix, our homotopy methods avoid inverting it. We have developed a code called CELLS/LIDS (CELLular Structures/Large Inelastic DeformationS), which provides the capabilities to study the variation of the mechanical properties of the low-mass metallic cellular structures by changing their topology. Thus, due to the efficiency of this method we can employ it for topology optimization design and for impact/energy absorption analyses.

1. Introduction

A lot of natural structures, such as hornbill bird beaks and bird wing bones, are architected cellular materials, which provide optimum strength and stiffness at low density. Humankind, over the past few years, has also fabricated cellular materials with more complex architectures in comparison with previously developed synthetic materials like open-cell metallic foams and honeycombs [Schaedler and Carter 2016]. Properties of these cellular structures are determined based on their parent materials and the topology of the microarchitecture. Additive manufacturing technologies and progress in three-dimensional (3D) printing techniques enable the design of materials and structures with complex cellular

microarchitectures, optimized for specific applications. In fact, one of the most interesting characteristics of cellular structures with pore networks is that they can be designed with desirable properties, making them appropriate for lightweight structures, metamaterials, energy absorption, thermal management, and bioscaffolds [Schaedler et al. 2014]. For example, efforts are under way to fabricate bioscaffolds to repair and replace tissue, cartilage, and bone [Hutmacher 2000; Mota et al. 2015; Valentin et al. 2006; Han and Gouma 2006]. These architected materials should be fabricated in such a way that they can meet biocompatibility requirements in addition to the mechanical properties of the tissues at the site of implantation. Therefore, presentation of a highly efficient computational method to predict and optimize the mechanical properties of such structures is of interest. Herein, we present a nearly exact and highly efficient computational method to predict the elastic-plastic homogenized mechanical properties of low-mass metallic systems with architected cellular microstructures. The framework of the methods presented in this paper is also germane to the analysis under static as well as impact loads, design, and topology optimization of cellular solids.

The ultralow-density metallic cellular microlattices have been recently fabricated at HRL Laboratories [Schaedler et al. 2011; Torrents et al. 2012], suitable for thermal insulation, battery electrodes, catalyst supports, and acoustic, vibration, or shock energy damping [Gibson and Ashby 1988; Evans et al. 2010; Lu et al. 2005; Valdevit et al. 2011; Ashby et al. 2000; Wadley 2002]. They produced nickel cellular microlattices, consisting of hollow tubular members, by preparing a sacrificial polymeric template for electroless Ni deposition, and then chemically etching the sacrificial template [Schaedler et al. 2011].

Using this process, they fabricated novel nickel-based microlattice materials with structural hierarchy spanning three different length scales: nm, μm and mm. They obtained a 93% Ni–7% P composition by weight for microlattices using energy dispersive spectroscopic analysis. They employed quasistatic axial compression experiments to measure macroscopic mechanical properties such as Young's moduli of nickel microlattices. The load P was measured by SENSOTEC load cells, and the displacement δ was measured using an external LVDT for modulus extraction. Strain-stress curves were obtained based on engineering stress and strain defined, respectively, as $\sigma = P/A_0$ and $\varepsilon = \delta/L_0$. A_0 and L_0 are the initial cross-sectional area and length of the sample, respectively.

Salari-Sharif and Valdevit [2014] extracted the Young's modulus of a series of nickel ultralight microlattices by coupling experimental results obtained using laser Doppler vibrometry with finite element (ABAQUS) simulations. Salari-Sharif and Valdevit [2014] fabricated a sandwich configuration by attaching carbon/epoxy face sheets as the top and bottom layers of the ultralight nickel hollow microlattice thin film [Schaedler et al. 2011]. Furthermore, Salari-Sharif and Valdevit [2014] detected the resonant frequencies by scanning laser vibrometry and ABAQUS simulations and extracted the relation between Young's modulus and the natural frequencies. Then, the effective Young's moduli of samples were obtained in the direction normal to the face sheets [Salari-Sharif and Valdevit 2014]. It is worth noting that for finite element (FE) modeling, a representative volume element (RVE) consisting of only four members of the cellular microlattice with at least ten thousand of 4-node shell FEs was employed [Salari-Sharif and Valdevit 2014], resulting in at least ten thousand nodes and, thus, sixty thousand degrees of freedom (DOF). We should emphasize that in our methodology each member can be modeled by a single spatial beam element. In other words, to perform a 4-member RVE analysis, we use only four spatial beam elements and five nodes, with a total of 30 DOF and, thus, at least 2000 times less DOF than in [Salari-Sharif and Valdevit 2014]. Since the cost of computation in a FE nonlinear analysis varies as the

n-th power (n between 2 and 3) of the number of DOF, it is clear that we seek to present a far more efficient analysis procedure than any available commercial software. This provides the capability to simulate the cellular microstructure using repetitive RVEs consisting of an arbitrary number of members, enabling a very efficient homogenization and/or direct numerical simulation (DNS) of a cellular macrostructure.

In addition, Schaedler et al. [2011] and Torrents et al. [2012] showed experimentally that nickel-phosphorous cellular microlattices undergo large effective compressive strains through extensive rotations about remnant node ligaments. Unfortunately, there are no computational studies in the literature on the large-deformation elastic-plastic analysis of such metallic cellular structures, which is the major concern of the present study, although there is a vast variety of studies on the large deformation analysis of space-frames [Besseling 1986; Geradin and Cardona 1988; Mallett and Berke 1966; Izzuddin 2001] from the era of large space structures for use in outer space. In the realm of space-frame analyses, numerous studies have been devoted to deriving an explicit expression for the tangent stiffness matrix of each element, accounting for arbitrarily large rigid rotations, moderately large nonrigid point-wise rotations, and the stretching-bending coupling [Bathe and Bolourchi 1979; Punch and Atluri 1984; Lo 1992; Kondoh et al. 1986; Kondoh and Atluri 1987]. Some researchers employed displacement-based approaches using variants of a Lagrangian for either geometrically or materially nonlinear analyses of frames [Bathe and Bolourchi 1979; Punch and Atluri 1984; Lo 1992]. Kondoh et al. [1986] extended the displacement approach to evaluate explicitly the tangent stiffness matrix without employing either numerical or symbolic integration for a beam element undergoing large deformations. Later, Kondoh and Atluri [1987] presented a formulation on the basis of assumed stress resultants and stress couples, satisfying the momentum balance conditions in the beam subjected to arbitrarily large deformations.

In order to study the elastic-plastic behavior of cellular members undergoing large deflections, we employ the mechanism of plastic hinge developed by Hodge [1959], Ueda et al. [1968], and Ueda and Yao [1982]. In this mechanism, a plastic hinge can be generated at any point along the member as well as its end nodes, anywhere the plasticity condition in terms of generalized stress resultants is satisfied. It is worthwhile to mention that contours of the von Mises stress given in [Salari-Sharif and Valdevit 2014] for the 4-member RVE with PBCs show a very high concentration of stress at the junction of four members. The stress contours were obtained based on linear elastic FE simulations [Salari-Sharif and Valdevit 2014]. Therefore, it clearly mandates an elastic-plastic analysis, which is undertaken in the present study. A complementary energy approach in conjunction with the plastic hinge method has been previously utilized to study elasto-plastic large deformations of space-framed structures [Kondoh and Atluri 1987; Shi and Atluri 1988]. Shi and Atluri [1988] derived the linearized tangent stiffness matrix of each finite element in the corotational reference frame in an explicit form and showed that this approach based on assumed stresses is simpler in comparison with assumed-displacement type formulations. In contrast to [Shi and Atluri 1988], which presents the linearized tangent stiffness, the current work derives explicitly the tangent stiffness matrix under the nonlinear coupling of axial, torsional, and bidirectional-bending deformations.

One of the extensively employed approaches in the literature for the analysis of nonlinear problems with large deformations or rotations is based on variational principles. For instance, Cai et al. [2009a; 2009b] utilized the primal approach as well as the mixed variational principle [Reissner 1953] in the updated Lagrangian corotational reference frame to obtain an explicit expression for the tangent stiffness matrix of the elastic beam elements. Cai et al. [2009a] showed that the mixed variational principle in

comparison to the primal approach, which requires C^1 continuous trial functions for displacements, needs simpler trial functions for the transverse bending moments and rotations. In fact, the authors assumed linear trial functions within each element and obtained much simpler tangent stiffness matrices for each element than those previously presented in the literature [Lo 1992; Kondoh et al. 1986; Simo 1985]. While Cai et al. [2009a] considered only a few macromembers, our analysis is applicable to metallic cellular microlattices with an extremely large number of repetitive RVEs. Since plasticity and buckling occur in many members of the microlattice, we found that the Newton-type algorithm that was utilized in [Cai et al. 2009a] fails. In the present study, we discovered that only our Newton homotopy method provides convergent solutions in the presence of the plasticity and buckling in a large number of members of the microlattice.

To solve tangent stiffness equations, we use a Newton homotopy method recently developed to solve a system of fully coupled nonlinear algebraic equations (NAEs) with as many unknowns as desired [Liu et al. 2009; Dai et al. 2014]. By using these methods, displacements of the equilibrium state are iteratively solved without the inversion of the Jacobian (tangent stiffness) matrix. Newton homotopy methods are advantageous, particularly when the effect of plasticity is going to be studied. It is well known that the simple Newton's method as well as the Newton–Raphson iteration method require the inversion of the Jacobian matrix, which fail to pass the limit load as the Jacobian matrix becomes singular, and require arc-length methodology which are commonly used in commercial off-the-shelf software such as ABAQUS. Furthermore, homotopy methods are useful in the following cases: when the system of algebraic equations is very large in size, when the solution is sensitive to the initial guess, and when the system of nonlinear algebraic equations is either over- or under-determined [Liu et al. 2009; Dai et al. 2014].

The paper is organized as follows. The theoretical background including the nonlinear coupling of axial, torsional, and bidirectional-bending deformations for a typical cellular member under large deformation; mixed variational principle in the corotational updated Lagrangian reference frame; the plastic hinge method; and the equation-solving algorithm accompanying Newton homotopy methods are summarized in Section 2. Section 3 is devoted to the validation of our methodology: a three-member rigid-knee frame, the Williams toggle problem, and a right-angle bent including the effect of plasticity are compared with the corresponding results given in the literature. Section 4 analyzes the mechanical behavior of two different cellular microlattices subjected to tensile, compressive, and shear loading. Throughout this section, it is shown that our calculated results (Young's modulus and yield stress) under compressive loading are very comparable with those measured experimentally by Schaedler et al. [2011] and Torrents et al. [2012]. Moreover, the progressive development of plastic hinges in the cellular microlattice as well as its deformed structure are presented. Finally, a summary and conclusion are given in Section 5. Appendices A, B, C, and D follow.

2. Theoretical background

Throughout this section, the concepts employed to derive nearly exact and highly efficient elastic-plastic homogenization of low-mass metallic systems with architected cellular microstructures are given. Nonlinear coupling of axial, torsional, and bidirectional-bending deformations; strain-displacement; and stress-strain relations in the updated Lagrangian corotational frame are described in Section 2.1. Section 2.2 is devoted to deriving an explicit expression for the tangent stiffness matrix of each member of the cellular

structure, accounting for large rigid rotations, moderate relative rotations, the bending-twisting-stretching coupling and elastic-plastic deformations. A solution algorithm is also given in Section 2.3.

2.1. *The nonlinear coupling of axial, torsional, and bidirectional-bending deformations for a spatial beam element with a tubular cross-section.* A typical 3D member of a cellular structure is considered, spanning between nodes 1 and 2 as illustrated in Figure 1. The element is initially straight with arbitrary cross section and is of the length l before deformation. As seen from Figure 1, three different coordinate systems are introduced:

(1) the global coordinates (fixed global reference) $\bar{x}_i$ with the orthonormal basis vectors $\bar{e}_i$,

(2) the local coordinates for the member in the undeformed state $\tilde{x}_i$ with the orthonormal basis vectors $\tilde{e}_i$, and

(3) the local coordinates for the member in the deformed state (current configuration) x_i with the orthonormal basis vectors of e_i $(i = 1, 2, 3)$.

Local displacements at the centroidal axis of the deformed member along e_i-directions are denoted as u_{i0}, $(i = 1, 2, 3)$. Rotation about x_1-axis (angle of twist) is denoted by $\hat{\theta}$, and those about x_i-axes, $i = 2, 3$, (bend angle) are denoted by θ_{i0}, $i = 2, 3$, respectively. It is assumed that nodes 1 and 2 of the member undergo arbitrarily large displacements, and rotations between the undeformed state of the member and its deformed state are arbitrarily finite. Moreover, it is supposed that local displacements in the current configuration (x_i coordinates system) are moderate and the axial derivative of the axial deflection at the centroid, $\partial u_{10}/\partial x_1$ is small in comparison with that of the transverse deflections at the centroid, $\partial u_{i0}/\partial x_1$ $(i = 2, 3)$.

We examine large deformations for a cylindrical member with an unsymmetrical cross section around x_2- and x_3-axes and constant cross section along x_1-axis subjected to torsion T around x_1-axis and bending moments M_2 and M_3 around x_2- and x_3-axes, respectively. It is assumed that the warping displacement $u_{1T}(x_2, x_3)$ due to the torsion T is independent of x_1 variable, the axial displacement at the centroid is $u_{10}(x_1)$, and the transverse bending displacements at the origin ($x_2 = x_3 = 0$) are $x_{20}(x_1)$ and
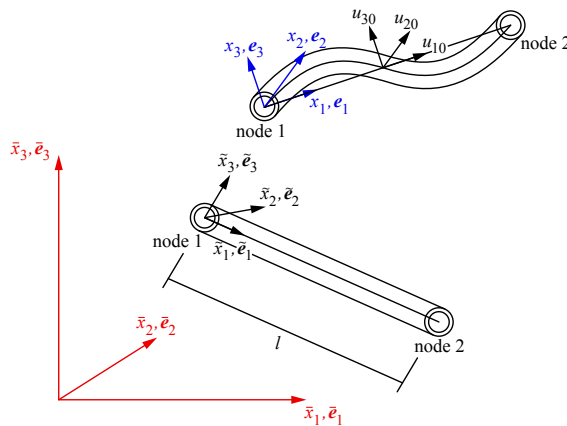

Figure 1. Nomenclature for the reference frames corresponding to the global, undeformed, and deformed states.

$x_{30}(x_1)$ along $\boldsymbol{e}_2$- and $\boldsymbol{e}_3$-directions, respectively. The reason for the consideration of the nonlinear axial, torsional, and bidirectional-bending coupling for each spatial beam element is the frame-like behavior of these cellular metallic microlattices. The scanning electron microscopy (SEM) images of microlattices given by Torrents et al. [2012] show the formation of partial fracture at nodes (for a microlattice with $t = 500$ nm), localized buckling (for a microlattice with $t = 1.3\,\mu$m), and plastic hinging at nodes (for a microlattice with $t = 26\,\mu$m). Therefore, the 3D displacement field for each spatial beam element in the current configuration is considered as follows using the normality assumption of the Bernoulli–Euler beam theory:

$$
\begin{aligned}
u_1(x_1, x_2, x_3) &= u_{1T}(x_2, x_3) + u_{10}(x_1) - x_2 \frac{\partial u_{20}(x_1)}{\partial x_1} - x_3 \frac{\partial u_{30}(x_1)}{\partial x_1}, \\
u_2(x_1, x_2, x_3) &= u_{20}(x_1) - \hat{\theta} x_3, \\
u_3(x_1, x_2, x_3) &= u_{30}(x_1) + \hat{\theta} x_2.
\end{aligned}
\tag{1}
$$

The Green–Lagrange strain components in the updated Lagrangian corotational frame $\boldsymbol{e}_i$ $(i = 1, 2, 3)$ are

$$
\varepsilon_{ij} = \tfrac{1}{2}(u_{i,j} + u_{j,i} + u_{k,i} u_{k,j}),
\tag{2}
$$

where the index notation $\bullet_{,i}$ denotes $\partial \bullet / \partial x_i$ and k is a dummy index. Replacement of (1) into (2) results in the following strain components:

$$
\begin{aligned}
\varepsilon_{11} &= u_{1,1} + \tfrac{1}{2}(u_{1,1})^2 + \tfrac{1}{2}(u_{2,1})^2 + \tfrac{1}{2}(u_{3,1})^2 \approx u_{10,1} + \tfrac{1}{2}(u_{20,1})^2 + \tfrac{1}{2}(u_{30,1})^2 - x_2 u_{20,11} - x_3 u_{30,11}, \\
\varepsilon_{22} &= u_{2,2} + \tfrac{1}{2}(u_{1,2})^2 + \tfrac{1}{2}(u_{2,2})^2 + \tfrac{1}{2}(u_{3,2})^2 = \tfrac{1}{2}(u_{1T,2} - u_{20,1})^2 + \tfrac{1}{2}\hat{\theta}^2 \approx 0, \\
\varepsilon_{33} &= u_{3,3} + \tfrac{1}{2}(u_{1,3})^2 + \tfrac{1}{2}(u_{2,3})^2 + \tfrac{1}{2}(u_{3,3})^2 \approx 0, \\
\varepsilon_{12} &= \tfrac{1}{2}(u_{1,2} + u_{2,1}) + \tfrac{1}{2} u_{3,1} u_{3,2} \approx \tfrac{1}{2}(u_{1T,2} - \hat{\theta}_{,1} x_3), \\
\varepsilon_{13} &= \tfrac{1}{2}(u_{1,3} + u_{3,1}) + \tfrac{1}{2} u_{2,1} u_{2,3} \approx \tfrac{1}{2}(u_{1T,3} + \hat{\theta}_{,1} x_2), \\
\varepsilon_{23} &= \tfrac{1}{2}(u_{2,3} + u_{3,2}) + \tfrac{1}{2} u_{1,2} u_{1,3} \approx 0.
\end{aligned}
\tag{3}
$$

By defining the following parameters:

$$
\begin{aligned}
\Theta &= \hat{\theta}_{,1}, \quad \mathfrak{N}_{22} = -u_{20,11}, \quad \mathfrak{N}_{33} = -u_{30,11}, \\
\varepsilon_{11}^0 &= u_{10,1} + \tfrac{1}{2}(u_{20,1})^2 + \tfrac{1}{2}(u_{30,1})^2 = \varepsilon_{11}^{0L} + \varepsilon_{11}^{0NL},
\end{aligned}
\tag{4}
$$

and employing them into (3), strain components can be rewritten as

$$
\begin{aligned}
\varepsilon_{11} &= \varepsilon_{11}^0 + x_2 \mathfrak{N}_{22} + x_3 \mathfrak{N}_{33}, \quad \varepsilon_{12} = \tfrac{1}{2}(u_{1T,2} - \Theta x_3), \\
\varepsilon_{13} &= \tfrac{1}{2}(u_{1T,3} + \Theta x_2), \quad\quad\quad\;\; \varepsilon_{22} = \varepsilon_{33} = \varepsilon_{23} = 0,
\end{aligned}
\tag{5}
$$

and in the matrix notation as

$$
\boldsymbol{\varepsilon} = \boldsymbol{\varepsilon}^L + \boldsymbol{\varepsilon}^N,
\tag{6}
$$

in which

$$\boldsymbol{\varepsilon}^L = \begin{bmatrix} \varepsilon_{11}^L \\ \varepsilon_{12}^L \\ \varepsilon_{13}^L \end{bmatrix} = \begin{bmatrix} u_{10,1} + x_2 \mathfrak{N}_{22} + x_3 \mathfrak{N}_{33} \\ \frac{1}{2}(u_{1T,2} - \Theta x_3) \\ \frac{1}{2}(u_{1T,3} + \Theta x_2) \end{bmatrix}, \tag{7}$$

$$\boldsymbol{\varepsilon}^N = \begin{bmatrix} \varepsilon_{11}^N \\ \varepsilon_{12}^N \\ \varepsilon_{13}^N \end{bmatrix} = \begin{bmatrix} \frac{1}{2}(u_{20,1})^2 + \frac{1}{2}(u_{30,1})^2 \\ 0 \\ 0 \end{bmatrix}. \tag{8}$$

Similarly, the member generalized strains are determined in the matrix form as

$$\boldsymbol{E} = \boldsymbol{E}^L + \boldsymbol{E}^N = \begin{bmatrix} \varepsilon_{11}^0 \\ \mathfrak{N}_{22} \\ \mathfrak{N}_{33} \\ \Theta \end{bmatrix}, \tag{9}$$

where $\boldsymbol{E}^L = [u_{10,1} \quad -u_{20,11} \quad -u_{30,11} \quad \hat{\theta}_{,1}]^T$ and $\boldsymbol{E}^N = [\frac{1}{2}(u_{20,1})^2 + \frac{1}{2}(u_{30,1})^2 \quad 0 \quad 0 \quad 0]^T$.

We consider for now that the member material is linear elastic, thus the total stress tensor (the second Piola–Kirchhoff stress tensor) $\boldsymbol{S}$ is calculated as

$$\boldsymbol{S} = \boldsymbol{S}^1 + \boldsymbol{\tau}^0. \tag{10}$$

Here $\boldsymbol{\tau}^0$ is the preexisting Cauchy stress tensor, and $\boldsymbol{S}^1$ is the incremental second Piola–Kirchhoff stress tensor in the updated Lagrangian corotational frame $\boldsymbol{e}_i$ given by

$$\begin{aligned} S_{11}^1 &= \mathrm{E}\,\varepsilon_{11}, & S_{12}^1 &= 2\mu\varepsilon_{12}, \\ S_{13}^1 &= 2\mu\varepsilon_{13}, & S_{22}^1 &= S_{33}^1 = S_{23}^1 \approx 0, \end{aligned} \tag{11}$$

in which μ is the shear modulus, $\mu = \mathrm{E}/(2(1+v))$, E is the elastic modulus, and v is the Poisson's ratio. Using (5) and (11), the generalized nodal forces for the member shown in Figure 1 subjected to the twisting and bending moments are calculated as

$$\begin{aligned} N_{11} &= \int_A S_{11}^1 \, \mathrm{d}A = E(A\varepsilon_{11}^0 + I_2 \mathfrak{N}_{22} + I_3 \mathfrak{N}_{33}), \\ M_{22} &= \int_A S_{11}^1 x_2 \, \mathrm{d}A = E(I_2 \varepsilon_{11}^0 + I_{22} \mathfrak{N}_{22} + I_{23} \mathfrak{N}_{33}), \\ M_{33} &= \int_A S_{11}^1 x_3 \, \mathrm{d}A = E(I_3 \varepsilon_{11}^0 + I_{23} \mathfrak{N}_{22} + I_{33} \mathfrak{N}_{33}), \\ T &= \int_A (S_{13}^1 x_2 - S_{12}^1 x_3) \, \mathrm{d}A = \mu I_{rr} \Theta, \end{aligned} \tag{12}$$

where A is the area of the cross section; I_i and I_{ij} $(i, j = 2, 3)$ are the first moment and the second moment of inertia of the cross section, respectively; $I_2 = \int_A x_2 \, \mathrm{d}A$, $I_3 = \int_A x_3 \, \mathrm{d}A$, $I_{22} = \int_A x_2^2 \, \mathrm{d}A$, $I_{33} = \int_A x_3^2 \, \mathrm{d}A$, $I_{23} = \int_A x_2 x_3 \, \mathrm{d}A$, and I_{rr} is the polar moment of inertia, $I_{rr} = \int_A (x_2^2 + x_3^2) \, \mathrm{d}A$. Using

the element generalized strains E the element generalized stresses σ are also determined in the matrix form as

$$\sigma = DE, \tag{13}$$

in which

$$\sigma = \begin{bmatrix} N_{11} \\ M_{22} \\ M_{33} \\ T \end{bmatrix}, \tag{14}$$

$$D = \begin{bmatrix} EA & EI_2 & EI_3 & 0 \\ EI_2 & EI_{22} & EI_{23} & 0 \\ EI_3 & EI_{23} & EI_{33} & 0 \\ 0 & 0 & 0 & \mu I_{rr} \end{bmatrix}. \tag{15}$$

2.2. Explicit derivation of tangent stiffness matrix undergoing large elasto-plastic deformation. In this section, the mixed variational principle in the corotational updated Lagrangian reference frame and a plastic hinge method are employed to obtain explicit expressions for the tangent stiffness matrix of each member shown in Figure 1. The stiffness matrix is calculated for each member by accounting for large rigid rotations; moderate relative rotations; the nonlinear coupling of axial, torsional, and bidirectional-bending deformations; and the effect of plasticity. The functional of the mixed variational principle in the corotational updated Lagrangian reference frame and the trial functions for the stress and displacement fields within each element are given in Section 2.2.1. Plastic analysis using the plastic hinge method is described in Section 2.2.2. The explicit expression of the stiffness matrix in the presence of plasticity for each cellular member is also presented in Section 2.2.3.

2.2.1. *Mixed variational principle in the corotational updated Lagrangian reference frame.* Consideration of S_{ij}^1 and u_i, respectively, as the components of the incremental second Piola–Kirchhoff stress tensor and the displacement field in the updated Lagrangian corotational frame, the functional of the mixed variational principle in the same reference frame with orthonormal basis vectors e_i is obtained as

$$\mathcal{H}_R = \int_V \left\{ -B[S_{ij}^1] + \tfrac{1}{2}\tau_{ij}^0 u_{k,i} u_{k,j} + \tfrac{1}{2} S_{ij}(u_{i,j} + u_{j,i}) - \rho b_i u_i \right\} dV - \int_{S_\sigma} \bar{T}_i u_i \, dS, \tag{16}$$

where V is the volume in the current corotational reference state, S_σ is the part of the surface with the prescribed traction, $\bar{T}_i = \bar{T}_i^0 + \bar{T}_i^1$ ($i = 1, 2, 3$) are the components of the boundary tractions, and $b_i = b_i^0 + b_i^1$ ($i = 1, 2, 3$) are the components of body forces per unit volume in the current configuration. The displacement boundary conditions prescribed at the surface S_u are also considered as $\bar{u}_i$ ($i = 1, 2, 3$), assumed to be satisfied a priori. Equation (16) is a general variational principle governing stationary conditions, which with respect to variations δS_{ij}^1 and δu_i results in the following incremental equations in the corotational updated Lagrangian reference frame:

$$\frac{\partial B}{\partial S_{ij}^1} = \tfrac{1}{2}(u_{i,j} + u_{j,i}), \tag{17}$$

$$[S_{ij}^1 + \tau_{ik}^0 u_{j,k}]_{,j} + \rho b_i^1 = -\tau_{ij,j}^0 - \rho b_i^0, \tag{18}$$

$$n_j[S_{ij}^1 + \tau_{ik}^0 u_{j,k}] - \bar{T}_i^1 = -n_j \tau_{ij}^0 + \bar{T}_i^0 \quad \text{on} \quad S_\sigma, \tag{19}$$

where $\boldsymbol{n}$ is the outward unit normal on the surface S_σ. For a group of members V_m ($m = 1, 2, \ldots, N$) with common surfaces ρ_m, (16) can be written as

$$\mathcal{H}_R = \sum_m \left(\int_{V_m} \left\{ -B[S_{ij}^1] + \tfrac{1}{2}\tau_{ij}^0 u_{k,i} u_{k,j} + \tfrac{1}{2}S_{ij}(u_{i,j} + u_{j,i}) - \rho b_i u_i \right\} \mathrm{d}V - \int_{S_{\sigma m}} \bar{T}_i u_i \, \mathrm{d}S \right),$$
$$m = 1, 2, \ldots, N. \tag{20}$$

If the trial function u_i and the test function ∂u_i for each member V_m ($m = 1, 2, \ldots, N$) are chosen in such a way that the interelement displacement continuity condition is satisfied at ρ_m a priori, then stationary conditions of $\mathcal{H}_R$ for a group of finite elements lead to

$$\partial B / \partial S_{ij}^1 = \tfrac{1}{2}(u_{i,j} + u_{j,i}) \quad \text{in} \quad V_m, \tag{21}$$

$$[S_{ij}^1 + \tau_{ik}^0 u_{j,k}]_{,j} + \rho b_i^1 = -\tau_{ij,j}^0 - \rho b_i^0 \quad \text{in} \quad V_m, \tag{22}$$

$$[n_i(S_{ij}^1 + \tau_{ik}^0 u_{j,k})]^+ + [n_i(S_{ij}^1 + \tau_{ik}^0 u_{j,k})]^- = -[n_i \tau_{ij}^0]^+ - [n_i \tau_{ij}^0]^- \quad \text{at} \quad \rho_m, \tag{23}$$

$$n_j[S_{ij}^1 + \tau_{ik}^0 u_{j,k}] - \bar{T}_i^1 = -n_j \tau_{ij}^0 + \bar{T}_i^0 \quad \text{on} \quad S_{\sigma m}. \tag{24}$$

Here, $+$ and $-$ denote the outward and inward quantities at the interface, respectively. The continuity of the displacement at the common interface ρ_m between elements is determined by

$$u_i^+ = u_i^- \quad \text{on} \quad \rho_m. \tag{25}$$

Applying (5) and (13) into (20) and integrating over the cross sectional area of each element gives

$$\mathcal{H}_R = \sum_{m=1}^N \left\{ \int_l \left(-\tfrac{1}{2}\boldsymbol{\sigma}^T \boldsymbol{D}^{-1} \boldsymbol{\sigma} \right) \mathrm{d}l + \int_l N_{11}^0 \tfrac{1}{2}(u_{20,1}^2 + u_{30,1}^2) \, \mathrm{d}l \right.$$
$$\left. + \int_l (\hat{N}_{11}\varepsilon_{11}^{0L} + \hat{M}_{22}\mathfrak{N}_{22} + \hat{M}_{33}\mathfrak{N}_{33} + \hat{T}\Theta) \, \mathrm{d}l - \bar{\boldsymbol{Q}}\boldsymbol{q} \right\}, \tag{26}$$

in which $\boldsymbol{\sigma}^0 = [N_{11}^0 \ M_{22}^0 \ M_{33}^0 \ T^0]^T$ is the initial member generalized stress in the corotational reference coordinates $\boldsymbol{e}_i$, $\hat{\boldsymbol{\sigma}} = \boldsymbol{\sigma} + \boldsymbol{\sigma}^0 = [\hat{N}_{11} \ \hat{M}_{22} \ \hat{M}_{33} \ \hat{T}]^T$ is the total member generalized stress in the coordinates $\boldsymbol{e}_i$, $\bar{\boldsymbol{Q}}$ is the nodal external generalized force vector in the global reference frame $\bar{\boldsymbol{e}}_i$, and $\boldsymbol{q}$ is the nodal generalized displacement vector in the coordinates $\bar{\boldsymbol{e}}_i$. Equation (26) can be simplified by applying integration by parts to the third integral term on the right-hand side of the equation. More details on how to perform the integration are given in Appendix A. Stationary conditions for $\mathcal{H}_R$ given in (26) result in

$$\boldsymbol{D}^{-1}\boldsymbol{\sigma} = \boldsymbol{E},$$
$$\hat{N}_{11,1} = 0 \quad \text{in } V_m,$$
$$\hat{T}_{,1} = 0 \quad \text{in } V_m, \tag{27}$$
$$\hat{M}_{22,11} + [N_{11}^0 u_{20,1}]_{,1} = 0 \quad \text{in } V_m,$$
$$\hat{M}_{33,11} + [N_{11}^0 u_{30,1}]_{,1} = 0 \quad \text{in } V_m,$$

and the nodal equilibrium equations are obtained from the following relation:

$$\sum_{m=1}^{N} \{\hat{N}_{11}\delta u_{10}|_0^l + \hat{M}_{22,1}\delta u_{20}|_0^l - \hat{M}_{22}\delta u_{20,1}|_0^l + \hat{M}_{33,1}\delta u_{30}|_0^l - \hat{M}_{33}\delta u_{30,1}|_0^l + \hat{T}\delta\hat{\theta}|_0^l$$
$$+ (N_{11}^0 u_{20,1})\delta u_{20}|_0^l + (N_{11}^0 u_{30,1})\delta u_{30}|_0^l - \bar{Q}\delta q\} = 0. \quad (28)$$

Herein, the trial functions for the stress and displacement fields within each member V_m ($m = 1, 2, \ldots, N$) are discussed. We assume that the components of the member generalized stress σ obey the following relation:

$$\sigma = P\beta, \quad (29)$$

where

$$P = \begin{bmatrix} 1 & 0 & 0 & 0 & 0 & 0 \\ 0 & -1+x_1/l & -x_1/l & 0 & 0 & 0 \\ 0 & 0 & 0 & 1-x_1/l & x_1/l & 0 \\ 0 & 0 & 0 & 0 & 0 & 1 \end{bmatrix}, \quad (30)$$

$$\beta = [n \ ^1m_3 \ ^2m_3 \ ^1m_2 \ ^2m_2 \ m_1]^T. \quad (31)$$

Similarly, the components of the initial member generalized stress σ^0 are determined as

$$\sigma^0 = P\beta^0, \quad (32)$$

where

$$\beta^0 = [n^0 \ ^1m_3^0 \ ^2m_3^0 \ ^1m_2^0 \ ^2m_2^0 \ m_1^0]^T. \quad (33)$$

Note that $^im_2(^im_2^0)$ and $^im_3(^im_3^0)$ are, respectively, bending moments (initial ones) around the x_2- and x_3-axes at the i-th node. Here, $n(n^0)$ and $m_1(m_1^0)$ are the (initial) axial force and the (initial) twisting moment along the element, respectively. Therefore, the incremental internal nodal force vector $\mathcal{B}$ for the element shown in Figure 1, with nodes 1 and 2 at the ends, can be expressed as

$$\mathcal{B} = [^1N \ ^1m_1 \ ^1m_2 \ ^1m_3 \ ^2N \ ^2m_1 \ ^2m_2 \ ^2m_3]^T, \quad (34)$$

which can be written as

$$\mathcal{B} = \mathfrak{R}\beta, \quad (35)$$

with

$$\mathfrak{R} = \begin{bmatrix} 1 & 0 & 0 & 0 & 0 & 0 \\ 0 & 0 & 0 & 0 & 0 & 1 \\ 0 & 1 & 0 & 0 & 0 & 0 \\ 1 & 0 & 0 & 0 & 0 & 0 \\ 0 & 0 & 0 & 0 & 0 & 1 \\ 0 & 0 & 0 & 0 & 1 & 0 \\ 0 & 0 & 1 & 0 & 0 & 0 \end{bmatrix}. \quad (36)$$

From (26), it is seen that only the squares of $u_{20,1}$ and $u_{30,1}$ appear within each member. Therefore, we assume the trial functions for the displacement field in such a way that $u_{20,1}$ and $u_{30,1}$ become linear for each member. Moreover, we suppose that the bend angles around the x_2- and x_3-axes along the member

shown in Figure 1 change with respect to the nodal rotations $^i\theta_{20}$ and $^i\theta_{30}$ ($i = 1, 2$) via the following relation:

$$\boldsymbol{u}_\theta = \boldsymbol{N}_\theta \boldsymbol{a}_\theta = \begin{bmatrix} 1 - x_1/l & 0 & x_1/l & 0 \\ 0 & 1 - x_1/l & 0 & x_1/l \end{bmatrix} \begin{bmatrix} ^1\theta_{20} \\ ^1\theta_{30} \\ ^2\theta_{20} \\ ^2\theta_{30} \end{bmatrix}. \tag{37}$$

Therefore, the nodal generalized displacement vector of the member can be expressed in the updated Lagrangian corotational frame $\boldsymbol{e}_i$ as

$$\boldsymbol{a} = [^1\boldsymbol{a} \quad ^2\boldsymbol{a}]^T, \tag{38}$$

where $^i\boldsymbol{a}$ ($i = 1, 2$) is the displacement vector of the i-th node:

$$^i\boldsymbol{a} = [^iu_{10} \quad ^iu_{20} \quad ^iu_{30} \quad ^i\hat{\theta} \quad ^i\theta_{20} \quad ^i\theta_{30}]^T. \tag{39}$$

The nodal generalized displacement vector of the member $\boldsymbol{a}$ is related to the vector $\boldsymbol{a}_\theta$ by

$$\boldsymbol{a}_\theta = \boldsymbol{T}_\theta \boldsymbol{a}, \tag{40}$$

in which

$$\boldsymbol{T}_\theta = \begin{bmatrix} 0 & 0 & 0 & 0 & 1 & 0 & 0 & 0 & 0 & 0 & 0 & 0 \\ 0 & 0 & 0 & 0 & 0 & 1 & 0 & 0 & 0 & 0 & 0 & 0 \\ 0 & 0 & 0 & 0 & 0 & 0 & 0 & 0 & 0 & 0 & 1 & 0 \\ 0 & 0 & 0 & 0 & 0 & 0 & 0 & 0 & 0 & 0 & 0 & 1 \end{bmatrix}. \tag{41}$$

Applying the trial functions of the stresses, (29) into the (26), the functional of the mixed variational principle in the corotational updated Lagrangian reference frame can be rewritten as

$$\mathcal{H}_R = -\mathcal{H}_{R1} + \mathcal{H}_{R2} + \mathcal{H}_{R3} - \mathcal{H}_{R4}. \tag{42}$$

Here,

$$\mathcal{H}_{R1} = \sum_{m=1}^N \int_l \left(\tfrac{1}{2}\boldsymbol{\sigma}^T \boldsymbol{D}^{-1} \boldsymbol{\sigma}\right) \mathrm{d}l = \sum_{m=1}^N \int_l \left(\tfrac{1}{2}\boldsymbol{\beta}^T \boldsymbol{P}^T \boldsymbol{C} \boldsymbol{P} \boldsymbol{\beta}\right) \mathrm{d}l, \tag{43}$$

$$\begin{aligned}
\mathcal{H}_{R2} &= \sum_{m=1}^N \Big\{ ^2N \, ^2u_{10} - {}^1N\,^1u_{10} + \tfrac{1}{l}(^1m_3 - {}^2m_3)(^2u_{20} - {}^1u_{20}) + {}^2m_3\,^2\theta_{30} - {}^1m_3\,^1\theta_{30} \\
&\qquad + \tfrac{1}{l}(^2m_2 - {}^1m_2)(^2u_{30} - {}^1u_{30}) + {}^2m_2\,^2\theta_{20} - {}^1m_2\,^1\theta_{20} + {}^2m_1\,^2\hat{\theta} - {}^1m_1\,^1\hat{\theta} \Big\} \\
&= \sum_{m=1}^N \{\boldsymbol{\mathcal{B}}^T \boldsymbol{\mathfrak{T}} \boldsymbol{a}\} = \sum_{m=1}^N \{\boldsymbol{\beta}^T \boldsymbol{\mathfrak{R}}^T \boldsymbol{\mathfrak{T}} \boldsymbol{a}\},
\end{aligned} \tag{44}$$

$$\begin{aligned}
\mathcal{H}_{R3} &= \sum_{m=1}^N \int_l N_{11}^0 \left[\tfrac{1}{2}(u_{20,1})^2 + \tfrac{1}{2}(u_{30,1})^2\right] \mathrm{d}l = \sum_{m=1}^N \int_l \sigma_1^0 \left[\tfrac{1}{2}(\theta_{20})^2 + \tfrac{1}{2}(\theta_{30})^2\right] \mathrm{d}l \\
&= \sum_{m=1}^N \int_l \tfrac{1}{2}\sigma_1^0 \boldsymbol{u}_\theta^T \boldsymbol{u}_\theta \, \mathrm{d}l = \sum_{m=1}^N \int_l \tfrac{1}{2}\sigma_1^0 \boldsymbol{a}^T \boldsymbol{A}_{nn} \boldsymbol{a} \, \mathrm{d}l,
\end{aligned} \tag{45}$$

$$\mathcal{H}_{R4} = \sum_{m=1}^{N}(\boldsymbol{a}^T\boldsymbol{F} - \boldsymbol{a}^T\mathfrak{T}^T\mathfrak{R}\boldsymbol{\beta}^0),\tag{46}$$

where

$$\boldsymbol{C} = \boldsymbol{D}^{-1},\tag{47}$$

$$\mathfrak{T} = \begin{bmatrix} -1 & 0 & 0 & 0 & 0 & 0 & 0 & 0 & 0 & 0 & 0 & 0 \\ 0 & 0 & 0 & -1 & 0 & 0 & 0 & 0 & 0 & 0 & 0 & 0 \\ 0 & 0 & 1/l & 0 & -1 & 0 & 0 & 0 & -1/l & 0 & 0 & 0 \\ 0 & -1/l & 0 & 0 & 0 & -1 & 0 & 1/l & 0 & 0 & 0 & 0 \\ 0 & 0 & 0 & 0 & 0 & 0 & 1 & 0 & 0 & 0 & 0 & 0 \\ 0 & 0 & 0 & 0 & 0 & 0 & 0 & 0 & 0 & 1 & 0 & 0 \\ 0 & 0 & -1/l & 0 & 0 & 0 & 0 & 0 & 1/l & 0 & 1 & 0 \\ 0 & 1/l & 0 & 0 & 0 & 0 & 0 & -1/l & 0 & 0 & 0 & 1 \end{bmatrix},\tag{48}$$

$$A_{nn} = \boldsymbol{T}_{\theta}^T \boldsymbol{N}_{\theta}^T \boldsymbol{N}_{\theta} \boldsymbol{T}_{\theta}.\tag{49}$$

Invoking the variational form for the functional of the mixed variational principle results in the following equation:

$$\sum_{m=1}^{N}\delta\boldsymbol{\beta}^T\left(-\int_l(\boldsymbol{P}^T\boldsymbol{C}\boldsymbol{P}\boldsymbol{\beta})\,\mathrm{d}l + \mathfrak{R}^T\mathfrak{T}\boldsymbol{a}\right) + \sum_{m=1}^{N}\delta\boldsymbol{a}^T\left(\mathfrak{T}^T\mathfrak{R}\boldsymbol{\beta} + \sigma_1^0\int_l A_{nn}\boldsymbol{a}\,\mathrm{d}l - \boldsymbol{F} + \mathfrak{T}^T\mathfrak{R}\boldsymbol{\beta}^0\right) = 0.\tag{50}$$

By letting $\boldsymbol{H} = \int_l \boldsymbol{P}^T\boldsymbol{C}\boldsymbol{P}\,\mathrm{d}l$, $\boldsymbol{G} = \mathfrak{R}^T\mathfrak{T}$, $\boldsymbol{K}_N = \sigma_0^1\int_l A_{nn}\,\mathrm{d}l$, $\boldsymbol{F}^0 = \boldsymbol{G}^T\boldsymbol{\beta}^0$, (50) can be rewritten as

$$\sum_{m=1}^{N}\delta\boldsymbol{\beta}^T(-\boldsymbol{H}\boldsymbol{\beta} + \boldsymbol{G}\boldsymbol{a}) + \sum_{m=1}^{N}\delta\boldsymbol{a}^T(\boldsymbol{G}^T\boldsymbol{\beta} + \boldsymbol{K}_N\boldsymbol{a} - \boldsymbol{F} + \boldsymbol{F}^0) = 0.\tag{51}$$

2.2.2. *Plasticity effects in the large deformation analysis of members of a cellular microstructure.* For an elastic-perfectly plastic material, the incremental work done on the material per unit volume is $\mathrm{d}w = \sigma_{ij}(\mathrm{d}\varepsilon_{ij}^p + \mathrm{d}\varepsilon_{ij}^e)$ in which ε_{ij}^e and ε_{ij}^p are elastic and plastic components of strain, respectively, and σ_{ij} are the stress components. Using the plastic hinge method, the plastic deformation is developed along the member wherever the plasticity condition is satisfied. Therefore, the total work expended in deforming the material of the body is

$$W = \int_V \sigma_{ij}(\mathrm{d}\varepsilon_{ij}^p + \mathrm{d}\varepsilon_{ij}^e)\,\mathrm{d}v = \int_V U(\varepsilon_{ij}^e)\,\mathrm{d}V + \sum_i \mathrm{d}W_i^p,\tag{52}$$

where $U(\varepsilon_{ij}^e)$ is the elastic strain energy density function, and $\mathrm{d}W_i^p$ is the increment of plastic work at the i-th plastic hinge. When the theory of plastic potential is applied, the plasticity condition in terms of the stress components at the i-th node is expressed as

$$f_i(\sigma_{xi}, \sigma_{yi}, \ldots, \tau_{xyi}, \ldots, \sigma_Y) = 0,\tag{53}$$

the increment of plastic work at the i-th node can be expressed as

$$dW_i^p = du^{p^T} x, \qquad (54)$$

in which du^p, the increment of plastic nodal displacement at the i-th node, is explained in terms of the function $f_i(x, \sigma_Y)$:

$$du^p = d\lambda_i \phi_i, \qquad (55)$$

$$\phi_i = \left[\frac{\partial f_i(x, \sigma_Y)}{\partial x} \right], \qquad (56)$$

where x is the nodal force, and $\delta\lambda_i$ is a positive scalar. Therefore, (52) can be rewritten as

$$W = \int_V U(\varepsilon_{ij}^e) \, dV + \sum d\lambda_i \phi_i^T \big|_{l_p} x, \qquad (57)$$

where $\hat{x}_l = l_p$ is the location of the plastic hinge. A variational form for the plastic work can be written as

$$\delta \left\{ \sum_{m=1}^{N} \left(\sum d\lambda_i \phi_i^T \big|_{l_p} \right) (P\beta^0 + P\beta) \right\} = \sum_{m=1}^{N} \delta \left(\sum d\lambda_i \phi_i^T \big|_{l_p} \right) (P\beta^0 + P\beta) + \left(\sum d\lambda_i \phi_i^T \big|_{l_p} \right) P\delta\beta$$

$$= \sum_{m=1}^{N} \sum \delta \, d\lambda_i \phi_i^T \big|_{l_p} (P\beta^0 + P\beta) + \left(\sum d\lambda_i \phi_i^T \big|_{l_p} \right) P\delta\beta$$

$$= \sum_{m=1}^{N} \sum \delta d\lambda_i \phi_i^T \big|_{l_p} (P\beta^0 + P\beta) + \delta\beta^T P^T \left(\sum d\lambda_i \phi_i^T \big|_{l_p} \right)^T. \qquad (58)$$

2.2.3. *Explicit derivation of tangent stiffness accompanying plasticity effects.* Using the functional of the mixed variational principle given in Section 2.2.1, (42)–(46), (57) is expressed as

$$W = \sum_{m=1}^{N} \left\{ -\int_l \left(\tfrac{1}{2} \beta^T P^T C P\beta \right) dl + (\beta^T \mathfrak{R}^T \mathfrak{T} a) + \int_l \tfrac{1}{2} \sigma_1^0 a^T T_\theta^T N_\theta^T N_\theta T_\theta a \, dl - (a^T F - a^T \mathfrak{T}^T \mathfrak{R}\beta^0) \right.$$

$$\left. + \left(\sum d\lambda_i \phi_i^T \big|_{l_p} \right) (P\beta^0 + P\beta) \right\}. \qquad (59)$$

Then, invoking $\delta W = 0$ and using (51) and (58), (51) can be modified to include the effect of plasticity by introducing new determined matrices $\hat{\beta}$, $\hat{H}$, and $\hat{G}$ by means of

$$\sum_{m=1}^{N} \delta\hat{\beta}^T (-\hat{H}\hat{\beta} + \hat{G}a) + \sum_{m=1}^{N} \delta a^T (\hat{G}^T \hat{\beta} + K_N a - F + F^0) = 0, \qquad (60)$$

with

$$\hat{\beta}^T = [\beta^T \ d\lambda], \qquad \hat{H} = \begin{bmatrix} H & A_{12} \\ A_{12}^T & 0 \end{bmatrix}, \qquad \hat{G}^T = [G^T \ 0], \qquad (61)\text{–}(63)$$

in which

$$A_{12}^T = \left[\frac{\partial f}{\partial N} \quad \frac{\partial f}{\partial \hat{M}_3} \left(-1 + \frac{l_p}{l} \right) \quad \frac{\partial f}{\partial \hat{M}_3} \left(-\frac{l_p}{l} \right) \quad \frac{\partial f}{\partial \hat{M}_2} \left(1 - \frac{l_p}{l} \right) \quad \frac{\partial f}{\partial \hat{M}_2} \frac{l_p}{l} \quad \frac{\partial f}{\partial \hat{M}_1} \right]. \tag{64}$$

Since $\delta \hat{\boldsymbol{\beta}}^T$ in (60) are independent and arbitrary in each element, we have

$$\hat{\boldsymbol{H}} \hat{\boldsymbol{\beta}} = \hat{\boldsymbol{G}} \boldsymbol{a}, \tag{65}$$

$$\hat{\boldsymbol{\beta}} = \hat{\boldsymbol{H}}^{-1} \hat{\boldsymbol{G}} \boldsymbol{a}. \tag{66}$$

By letting $\sum_{m=1}^N \delta \boldsymbol{a}^T (\hat{\boldsymbol{G}}^T \hat{\boldsymbol{\beta}} + \boldsymbol{K}_N \boldsymbol{a} - \boldsymbol{F} + \boldsymbol{F}^0) = 0$ and substituting $\hat{\boldsymbol{\beta}}$ from (66), we obtain

$$(\hat{\boldsymbol{G}}^T \hat{\boldsymbol{H}}^{-1} \hat{\boldsymbol{G}} + \boldsymbol{K}_N) \boldsymbol{a} - \boldsymbol{F} + \boldsymbol{F}^0 = 0, \tag{67}$$

Therefore, the stiffness matrix $\mathcal{K}$ in the presence of plasticity is derived explicitly as

$$\mathcal{K} = \hat{\boldsymbol{G}}^T \hat{\boldsymbol{H}}^{-1} \hat{\boldsymbol{G}} + \boldsymbol{K}_N = \boldsymbol{G}^T \boldsymbol{H}^{-1} \boldsymbol{G} + \boldsymbol{K}_N - \boldsymbol{G}^T \boldsymbol{H}^{-1} \boldsymbol{A}_{12} \boldsymbol{C}^T \boldsymbol{G} = \boldsymbol{K} - \boldsymbol{G}^T \boldsymbol{H}^{-1} \boldsymbol{A}_{12} \boldsymbol{C}^T \boldsymbol{G} = \boldsymbol{K} - \boldsymbol{K}_P, \tag{68}$$

where

$$\boldsymbol{K} = \boldsymbol{G}^T \boldsymbol{H}^{-1} \boldsymbol{G} + \boldsymbol{K}_N = \boldsymbol{K}_L + \boldsymbol{K}_N, \tag{69}$$

$$\boldsymbol{K}_P = \boldsymbol{G}^T \boldsymbol{H}^{-1} \boldsymbol{A}_{12} \boldsymbol{C}^T \boldsymbol{G}, \tag{70}$$

$$\boldsymbol{C}^T = (\boldsymbol{A}_{12}^T \boldsymbol{H}^{-1} \boldsymbol{A}_{12})^{-1} \boldsymbol{A}_{12}^T \boldsymbol{H}^{-1}. \tag{71}$$

Since we are studying the nonlinear coupling of axial, torsional, and bidirectional-bending deformations for each element, the plasticity condition is introduced by $f_i(N, \hat{M}_1, \hat{M}_2, \hat{M}_3) = 0$ at the location of the i-th plastic hinge; then

$$\boldsymbol{\phi}_i = \left[\frac{\partial f_i}{\partial N} \quad \frac{\partial f_i}{\partial \hat{M}_1} \quad \frac{\partial f_i}{\partial \hat{M}_2} \quad \frac{\partial f_i}{\partial \hat{M}_3} \right]^T \tag{72}$$

and

$$\sum d\lambda_i \boldsymbol{\phi}_i^T \big|_{l_p} = \left[\sum d\lambda_i \frac{\partial f_i}{\partial N} \big|_{l_p} \quad \sum d\lambda_i \frac{\partial f_i}{\partial \hat{M}_1} \big|_{l_p} \quad \sum d\lambda_i \frac{\partial f_i}{\partial \hat{M}_2} \big|_{l_p} \quad \sum d\lambda_i \frac{\partial f_i}{\partial \hat{M}_3} \big|_{l_p} \right]$$

$$= [H_P \quad \theta_{P1}^* \quad \theta_{P2}^* \quad \theta_{P3}^*], \tag{73}$$

in which H_P is the plastic elongation and θ_{Pi}^*, $i = (1, 2, 3)$ are the plastic rotations at the location of plastic hinges. Components of the element tangent stiffness matrices, $\boldsymbol{K}_N$, $\boldsymbol{K}_L$, and $\boldsymbol{K}_P$, are presented in Appendix B. Transformation matrices relating coordinate systems corresponding to the deformed and undeformed states to the global coordinates system (Figure 1) are given in Appendix C.

2.3. *Solution algorithm.* To solve the incremental tangent stiffness equations, we employ a Newton homotopy method [Liu et al. 2009; Dai et al. 2014]. One of the most important reasons that we use the newly developed scalar homotopy method is that this approach does not need to invert the Jacobian matrix (the tangent stiffness matrix) to solve NAEs. In the case of complex problems (such as elastic-plastic analyses of large deformations and near the limit-load points in post-buckling analyses of geometrically nonlinear frames) where the Jacobian matrix may be singular, the iterative Newton's methods become problematic and necessitate the use of arc-length methods found in software such as ABAQUS.

One of the other advantages of the recently developed homotopy methods is the improved performance over the Newton–Raphson method when the Jacobian matrix is nearly singular or is severely ill-conditioned. For instance, when we considered the problem discussed in Section 3.1 (three-member rigid-knee frame) using the Newton–Raphson algorithm, the provided code couldn't converge to capture the critical load, while it converged rapidly after switching to the homotopy algorithm. Moreover, we discovered that while the Newton-type algorithm fails to converge, the Newton homotopy method provides convergent solutions in the presence of plasticity and buckling in a large number of members of the microlattice. As another benefit of the employed algorithm, our developed CELLS/LIDS code is not sensitive to the initial guess of the solution vector, unlike the Newton–Raphson method.

The homotopy method was first introduced by Davidenko [1953] to enhance the convergence rate from a local convergence to a global one for the solution of the NAEs of $F(X) = 0$; where $X \in \mathbb{R}^n$ is the solution vector. This methodology was based on the employment of a vector homotopy function $H(X, t)$ to continuously transform a function $G(X)$ into $F(X)$. The variable t ($0 \leq t \leq 1$) was the homotopy parameter, treated as a time-like fictitious variable, and the homotopy function was any continuous function such that $H(X, 0) = 0 \Leftrightarrow G(X) = 0$ and $H(X, 1) = 0 \Leftrightarrow F(X) = 0$. More details on the vector homotopy functions are given in Appendix D. To improve the vector homotopy method, Liu et al. [2009] proposed a scalar homotopy function $h(X, t)$ such that $h(X, 0) = 0 \Leftrightarrow \|G(X)\| = 0$ and $h(X, 1) = 0 \Leftrightarrow \|F(X)\| = 0$. They introduced the following scalar fixed-point homotopy function:

$$h(X, t) = \tfrac{1}{2}(t\|F(X)\|^2 - (1 - t)\|X - X_0\|^2), \quad 0 \leq t \leq 1. \tag{74}$$

Later, Dai et al. [2014] suggested more convenient scalar homotopy functions which hold for $t \in [0, \infty)$ instead of $t \in [0, 1]$. We consider the following scalar Newton homotopy function to solve the system of equations $F(X) = 0$:

$$h_n(X, t) = \tfrac{1}{2}\|F(X)\|^2 + \frac{1}{2Q(t)}\|F(X_0)\|^2, \quad t \geq 0, \tag{75}$$

resulting in

$$\dot{X} = -\frac{1}{2}\frac{\dot{Q}\|F\|^2}{Q\|B^T F\|^2}B^T F, \quad t \geq 0, \tag{76}$$

where B is the Jacobian (tangent stiffness) matrix evaluated with $B = \partial F/\partial X$ and $Q(t)$ is a positive and monotonically increasing function to enhance the convergence speed. Various possible choices of $Q(t)$ can be found in [Dai et al. 2014]. Finally, the solution vector X can be obtained by numerically integrating (76) or using iterative Newton homotopy methods discussed in Appendix D.

3. Representative approach and its validation

This section is devoted to considering the validity of our proposed methodology. To this end, three different problems are analyzed and compared with results from other methods given in the literature. The critical load of the three-member rigid-knee frame is computed in Section 3.1. Section 3.2 examines the classical Williams toggle problem. Section 3.3 is devoted to considering the accuracy and efficiency of the calculated stiffness matrix in the presence of plasticity by solving the problem of the right-angle bent.
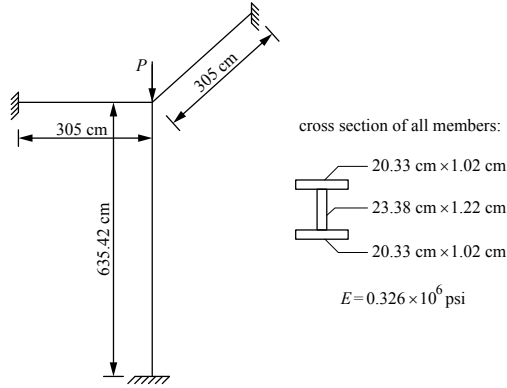
Figure 2. The geometry of three-member rigid-knee frame and the cross section of elements.
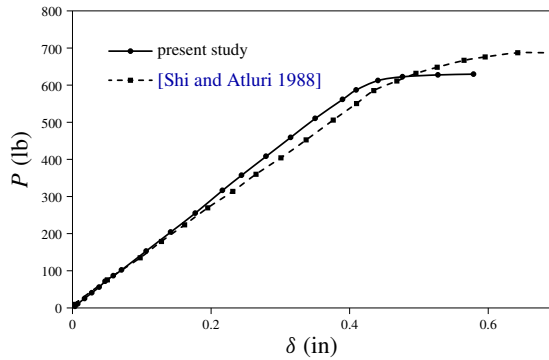

Figure 3. Load versus displacement at the location of point load.

3.1. *Three-member rigid-knee frame.* The geometry of the three-member rigid-knee frame and the cross section of elements are shown in Figure 2. Using the CELLS/LIDS (CELLular Structures/Large Inelastic DeformationS) code, the longer element is divided into 6 elements and shorter elements are divided into 3 elements. A transverse perturbation loading $0.001P$ is also applied at the midpoint of the longer member. Load versus displacement at the location of point load is plotted in Figure 3 and is compared with the corresponding results presented by Shi and Atluri [1988]. As it is observed, there is a good agreement between present calculated results and those obtained in [Shi and Atluri 1988]. Please note that Shi and Atluri [1988] have also mentioned that their computed critical load is a little higher than that obtained by Mallett and Berke [1966].

3.2. *Classical Williams toggle problem.* Williams [1964] developed a theory to study the behavior of the members of a rigid jointed plane framework and applied it to the case of the rigid jointed toggle. The classical toggle problem is exhibited in Figure 4, consisting of two rigidly jointed elements with equal lengths L and anchored at their remote ends. The angle between the element and the horizontal axis b is related to the length of the elements via the relation $L \sin(b) = 0.32$. The characteristics of the cross section of elements are also included in Figure 4. The structure is subjected to an external load W along the z-direction at the apex, as illustrated in Figure 4. The deflection of the apex versus the applied
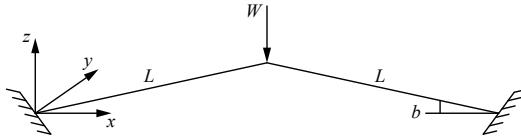
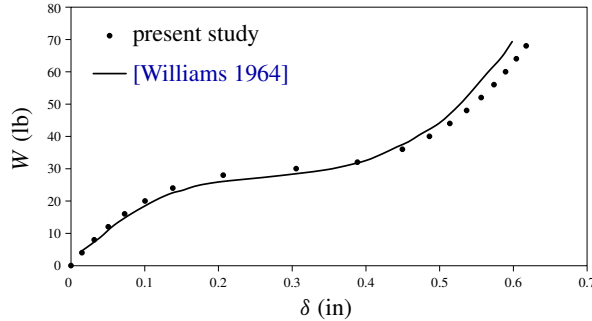**Figure 4.** Classical toggle problem.

Figure 5. Displacement at the apex of toggle versus the applied load.

load is calculated and compared with results given by Williams [1964] in Figure 5. As it is seen, good correspondence is obtained.

3.3. *Elastic-plastic right-angle bent.* Throughout this section, the accuracy and efficiency of our methodology to consider the effect of plasticity is investigated. To this end, the problem of right-angle bent is calculated and compared with the results from other works. Two equal members of length l with square cross sections are located in the xy-plane and are subjected to an external load F along the z-direction at the midpoint of one element, as shown in Figure 6. Both members are anchored at their remote ends. Therefore, they are under both bending M and twisting T. The yielding condition for such a perfectly plastic material subjected to bending and twisting is $(M/M_0)^2 + (T/T_0)^2 = 1$, in which M_0 and T_0 are, respectively, fully plastic bending and twisting moments. Employing our CELLS/LIDS code, each member is simulated by four elements. The formation of plastic hinges via the increase of external load is presented in Figure 6 and the calculated amounts of Fl/M_0 at the onset of plastic hinges are compared with the results given by Shi and Atluri [1988]. The variation of $\delta \times EI/(M_0 l^2)$ with respect to Fl/M_0 is also plotted in Figure 7. Here, δ is the displacement of the tip of the right-angle bent along the z-direction, and E is the Young's modulus. The results also show good agreement with those in [Hodge 1959].

4. Low-mass metallic systems with architected cellular microstructures

This section is devoted to the computational study of large elastic-plastic deformations of the nickel-based cellular microlattices fabricated at HRL Laboratories [Schaedler et al. 2011; Torrents et al. 2012]. To mimic the fabricated cellular microstructures, we model repetitive RVEs constructed by the strut members with the same geometry and dimension as the experiment. Each member of the actual cellular microstructure undergoing large elastic-plastic deformations is modeled by a single spatial beam finite element with 12 DOF, providing the capability to decrease considerably the number of DOF in comparison with the same simulation using commercial FE software. The strut members are connected in such
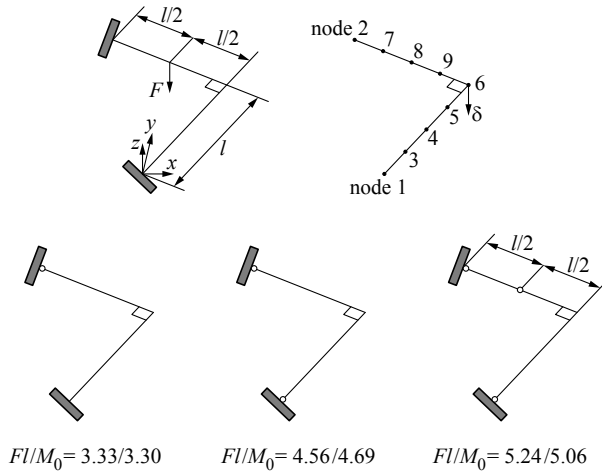
Figure 6. Progressive development of plastic hinges in the right-angle bent. The first number in the Fl/M_0 sets is from the present study, and the second is from [Shi and Atluri 1988].
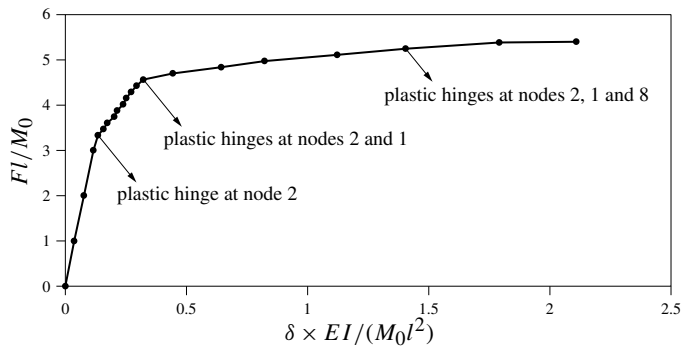

Figure 7. The variation of normalized load with respect to the normalized displacement at the tip of right-angle bent.

a way that the topology of the fabricated cellular material is achieved. In the following, more details on the formation of RVE mimicking the actual microstructural samples are given. The properties of nickel as the parent material of the architected material is introduced within the CELLS/LIDS code by the Young's modulus $E^s = 200$ GPa and the yield stress $\sigma_y^s = 450$ MPa. The considered RVE is a Bravais lattice formed by repeating octahedral unit cells without any lattice members in the basal plane, as shown in Figure 8. The lattice constant parameter of the unit cell is a; see Figure 8. The RVE is constructed by a node-strut representation and includes the nodes coordinate and the nodes connectivity, which determines the length of the members as well as the topology of the microlattice. Furthermore, the present RVE approach accurately captures the microstructural length scale by introducing the area, the first and the second moments of inertia, and the polar moment of inertia of the symmetrical/unsymmetrical cross section of the hollow tube member within the formulation. Periodic boundary conditions (PBCs) are considered along the x- and y-directions of the RVE, which are the directions perpendicular to the depth
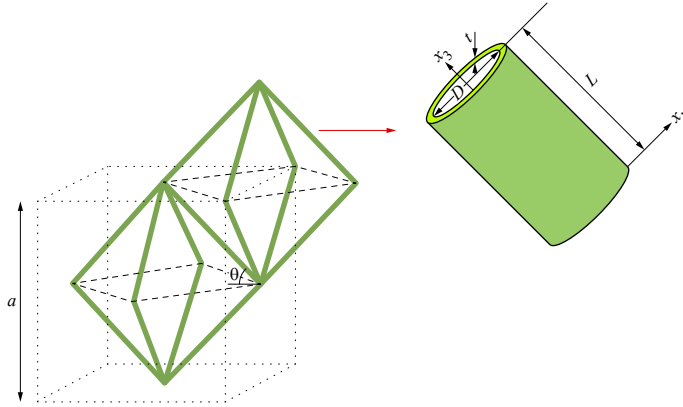
Figure 8. The unit cell of RVE consisting of an octahedron as well as the geometry of strut members.

of the thin film microlattice. PBCs are involved by ${}^{i}\boldsymbol{a}|_{x=0} = {}^{j}\boldsymbol{a}|_{x=na}$ along the x-direction and by ${}^{k}\boldsymbol{a}|_{y=0} = {}^{l}\boldsymbol{a}|_{y=ma}$ along the y-direction, in which ${}^{\alpha}\boldsymbol{a}(\alpha = i, j, k, l)$ is the displacement vector of the α-th node (39) on the boundary of the RVE, and n or m is determined based on the size of the RVE along the x- or y-direction, respectively. For example, for the $Na \times Ma \times Ka$ RVE, $n = N$ and $m = M$. The depth of the RVE is modeled to be equal to the thickness of the thin film. Section 4.1 studies the $1a \times 1a \times 2a$ RVE including 20 nodes and 32 strut members, and Section 4.2 examines both the $2a \times 2a \times 2a$ RVE with 60 nodes and 128 strut members and the $1a \times 1a \times 4a$ RVE with 36 nodes and 64 members. We study the mechanical behavior of the thin film cellular microlattice under tension, compression, and shear loadings. To this end, nodes on both the top and bottom faces of the RVE are loaded accordingly. Microlattice members are cylindrical hollow tubes, the dimensions of which are also included in Figure 8. Torrents et al. [2012] tested samples with the strut member length of $L = 1$–$4\,\mathrm{mm}$, strut member diameter of $D = 100$–$500\,\mu\mathrm{m}$, wall thickness of $t = 100$–$500\,\mathrm{mm}$, and inclination angle of $\theta = 60°$. In Sections 4.1 and 4.2, we analyze the mechanical behavior of two different fabricated cellular microlattices in which the geometry of their strut members (L, D, t, and θ) are explained, respectively. Since nonlinear coupling of axial, torsional, and bidirectional-bending deformations is considered for each member, the plasticity condition is determined by the following relation:

$$f(N_{11}, M_{22}, M_{33}, T) = \frac{1}{M_0}\{M_{22}^2 + M_{33}^2 + T^2\}^{1/2} + \frac{N_{11}^2}{N_0^2} - 1 = 0, \qquad (77)$$

where M_0 and N_0 are the fully plastic bending moment and fully plastic axial force, respectively.

4.1. *Architected material with more flexibility as compared to parent material.* An RVE including 20 nodes and 32 members with PBCs along the x- and y-directions is employed to model a cellular thin film with the thickness of $2a$; see Figure 9. This figure shows the application of the external compressive loading, which changes according to tensile as well as shear loads. The dimensions of each member in the microlattice is as follows: $L = 1050\,\mu\mathrm{m}$, $D = 150\,\mu\mathrm{m}$, and $t = 500\,\mathrm{nm}$.

The engineering stress as a function of the engineering strain is presented in Figure 10 for the nickel cellular microlattice under compressive, tensile, and shear loads. The stress-strain curves corresponding
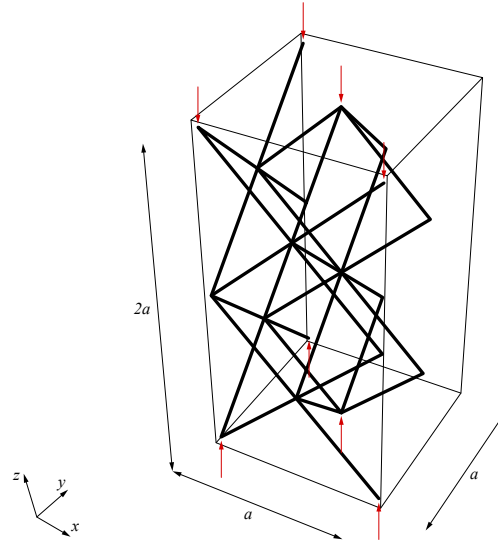
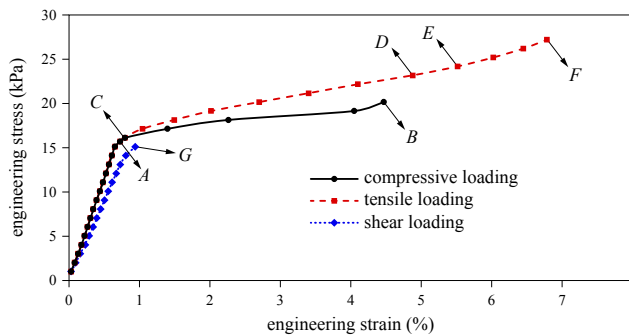**Figure 9.** $1a \times 1a \times 2a$ RVE including 20 nodes and 32 strut members.

Figure 10. Stress-strain curve of the cellular microlattice subjected to tension, compression, and shear.

to the tensile and compressive loads result in the overall yield stress of the RVE $\sigma_y = 15.117$ kPa and the Young's modulus $E = 2.291$ MPa. Torrents et al. [2012] measured the respective values $\sigma_y = 14.2 \pm 2.5$ kPa and $E = 1.0 \pm 0.15$ MPa for their tested microlattice labeled with G ($L = 1050 \pm 32\,\mu$m, $D = 160 \pm 24\,\mu$m, $t = 0.55 \pm 0.06\,\mu$m). The results calculated from our computational methodology agree excellently with those obtained from experiment by Torrents et al. [2012]. It is found that this architected material shows a yield stress much smaller than the parent material, which offers more flexibility in tailoring the response to impulsive loads. In addition, we are able to calculate the shear modulus of the cellular microlattice from our obtained stress-strain curve corresponding to the shear load, resulting in $G = 1.773$ MPa.

The progressive development of plastic hinges as the tensile and compressive loads increase is shown in Figure 11. The total deformation of the RVE considering the effect of plasticity corresponding to the step B of compressive loading, step F of tensile loading, and step G of shear loading is also given in
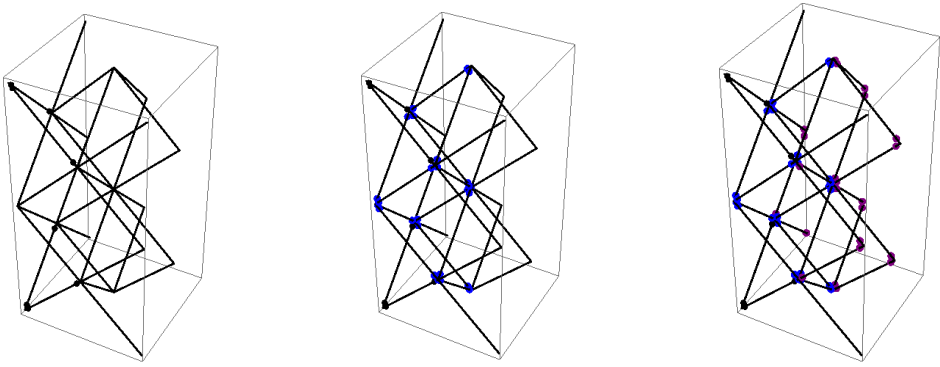
Figure 11. Progressive development of plastic hinges in cellular microlattice under tension and compression at different steps of loading shown in Figure 10. Left: plastic hinges formed at steps A and C. Middle: plastic hinges formed at steps B and D. Right: plastic hinges formed at step E.
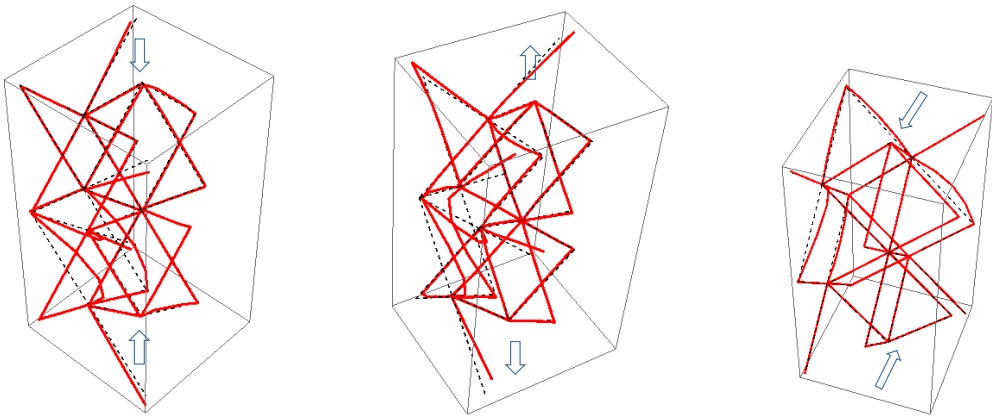

Figure 12. Total elastic-plastic deformation of the cellular microstructure in red color at different steps of loading shown in Figure 10. Left: at step B of the compressive loading. Middle: at step F of the tensile loading. Right: at the step G of shear loading. The initial unloaded state is also shown (dashed lines).

Figure 12. Since plastic deformation can absorb energy, this architected material will be appropriate for protection from impacts and shockwaves in applications varying from helmets to vehicles and sporting gear [Schaedler and Carter 2016].

4.2. *Architected material with further increased relative density.* In this case, the fabricated sample is computationally modeled using an RVE consisting of 60 nodes and 128 members with PBCs along the x- and y-directions; see Figure 13. The strut member dimensions are $L = 1200\,\mu$m, $D = 175\,\mu$m and $t = 26\,\mu$m. The wall thickness of the member in this case is 52 times greater than that of the previous case in Section 4.1. The RVE is subjected to both tensile and compressive loading in order to study the mechanical properties of the architected material. The engineering stress-engineering strain
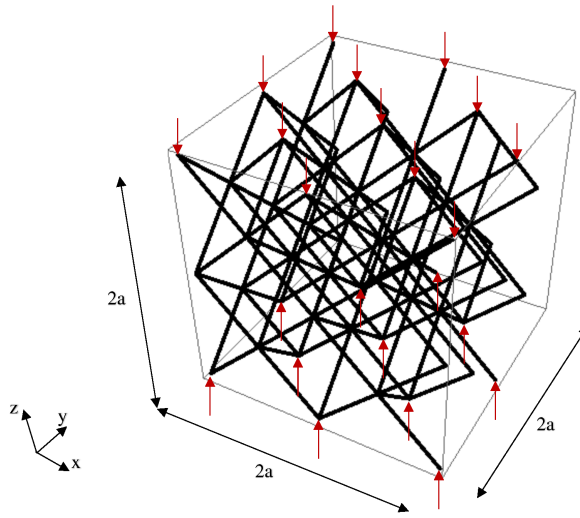
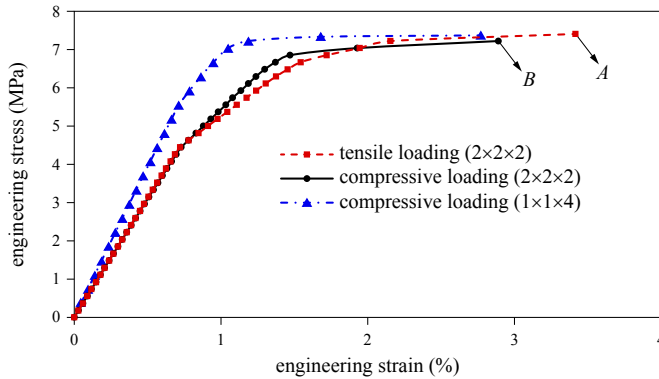**Figure 13.** $2a \times 2a \times 2a$ RVE including 60 nodes and 128 strut members.

Figure 14. Stress-strain curve of the cellular microlattice subjected to tension and compression.

curve is plotted in Figure 14. Stress analysis shows bilinear elastic moduli for this cellular microlattice subjected to both tension and compression. Elastic modulus for the first phase is calculated as 0.619 GPa under both tensile and compressive loading. For the second phase it is calculated to be 0.284 GPa under tension and 0.364 GPa under compression. The yield stress is obtained as 7.2222 MPa and 6.8519 MPa subjected to tensile and compressive loading, respectively. Plastic hinges emanate at the stress level 6.6667 MPa when the microlattice is under tension and originate at the stress level 6.8519 MPa when the microlattice is subjected to compression. It is found that both Young's modulus and the yield stress of the cellular microlattice increase significantly by increasing the strut thickness. It is well-known that the elastic modulus and the yield strength of the cellular materials increase with the increase of their relative density [Gibson and Ashby 1988]. Relative density is calculated as ρ/ρ_s, where ρ is the mass of the lattice divided by the total bounding volume v and ρ_s is the mass of the lattice divided by only the volume of the constituent solid material v_s. Therefore, $\rho/\rho_s = (m/v)/(m/v_s) = v_s/v$ in which $v_s = $ # of members $\times \pi\left[\left(\frac{1}{2}D + t\right)^2 - \left(\frac{1}{2}D\right)^2\right] \times L$ and $v = 8a^3$ or $2a^3$ for a $2a \times 2a \times 2a$ RVE or a $1a \times 1a \times 2a$ RVE,
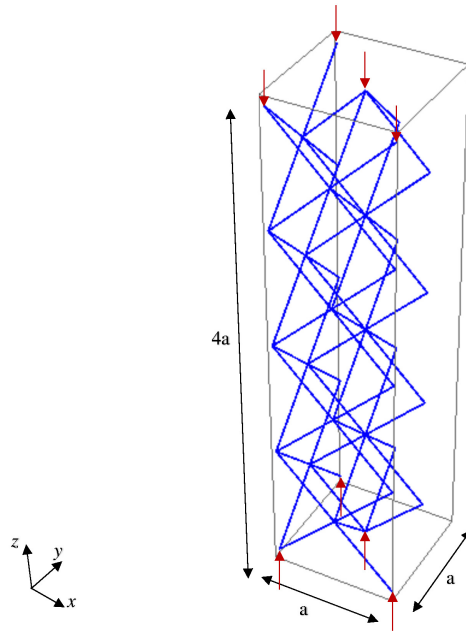
Figure 15. $1a \times 1a \times 4a$ RVE consisting of 36 nodes and 64 strut members.

respectively. We calculate the relative densities of the cellular microlattices examined through this section and Section 4.1 as 0.03511 and 0.00066, respectively. Torrents et al. [2012] extracted experimentally the strain-stress curve of this microlattice (labeled A) under compression. They measured the Young's modulus $E = 0.58 \pm 0.003$ GPa and the yield stress $\sigma_y = 8.510 \pm 0.025$ MPa for the tested microlattice with strut diameter $D = 175 \pm 26 \, \mu$m, strut length $L = 1200 \pm 36 \, \mu$m, and wall thickness $t = 26.00 \pm 2.6 \, \mu$m. We see that there is a very good correspondence between our calculated mechanical properties of the sample under compressive loading and those measured experimentally by Torrents et al. [2012].
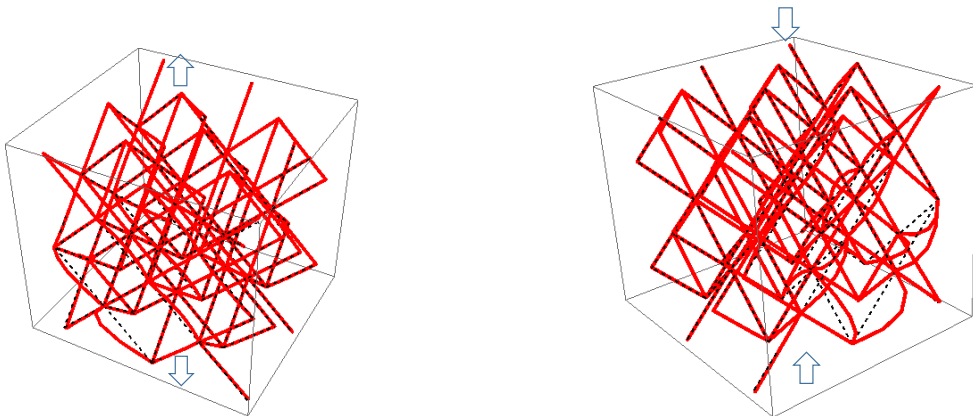

Figure 16. Elastic-plastic deformation of the cellular microstructure in red color at different steps of loading shown in Figure 14. Left: at step A of tensile loading. Right: at step B of compressive loading. The initial unloaded state is also shown (dashed lines).

To investigate the effect of the size of the RVE on the macroscale response of the cellular microlattice, the depth of the $2a \times 2a \times 2a$ RVE (Figure 13) is increased by a factor of two. Due to the PBCs along the x- and y-directions, the size of the RVE along these directions is considered to be $1a$. Therefore, a $1a \times 1a \times 4a$ RVE consisting of 36 nodes and 64 strut members is modeled (see Figure 15), and the corresponding stress-strain curve under compression is included in Figure 14. The stress analysis of this $1a \times 1a \times 4a$ RVE also exhibits bilinear elastic behavior with the elastic moduli of 0.7841 GPa for the first linear phase and 0.4721 GPa for the second linear phase. The yield stress is calculated to be 7.3704 MPa, which comes closer to the corresponding experimental value, $\sigma_y = 8.510 \pm 0.025$ MPa, in comparison with 6.8519 MPa calculated for a $2a \times 2a \times 2a$ RVE. Figure 16 shows the elastic-plastic deformation of the $2a \times 2a \times 2a$ RVE under tension and compression.

5. Conclusion

We presented a computational approach for the large elastic-plastic deformation analysis of low-mass metallic systems with architected cellular microstructures. Studies on this class of materials are of interest since they can be optimized for specific loading conditions by changing the base material as well as the topology of the architecture. The repetitive RVE approach is utilized to mimic the fabricated cellular microlattices. The RVE is generated by a node-strut representation consisting of the coordinate of nodes and the connectivity of nodes. Therefore, we can easily study the effect of the change of topology on the overall mechanical response of the cellular material by changing both the coordinates and connectivity of nodes. Moreover, the microstructural length scale of the cellular material is accurately captured by introducing the area, the first and the second moments of inertia, and the polar moment of inertia of the symmetrical/unsymmetrical cross section of the strut member within the formulation.

In the current methodology, each member of the actual microlattice undergoing large elastic-plastic deformations is modeled by a single FE with 12 DOF, which enables the study of the static and dynamic behavior of the macrostructure directly and efficiently by using an arbitrarily large number of members. We study the nonlinear coupling of axial, torsional, and bidirectional-bending deformations for each 3D spatial beam element. The effect of plasticity is included by employing the plastic hinge method, and the tangent stiffness matrix is explicitly derived for each member, utilizing the mixed variational principle in the updated Lagrangian corotational reference frame. To avoid inverting the Jacobian matrix, we employ homotopy methods to solve the incremental tangent stiffness equations.

The proposed methodology is validated by comparing the results of the elastic and elastic-plastic large deformation analyses of some problems with the corresponding results given in the literature. Moreover, two fabricated cellular microlattices with different dimensional parameters including the unit cell size and the strut thickness are modeled using different RVEs. We study their mechanical behaviors under all tensile, compressive, and shear loading. The comparison of the calculated mechanical properties utilizing the present methodology with the corresponding experimental measurements available in the literature reveals a very good agreement. Using this developed computational approach, we can homogenize any cellular structure easily, and we can design the topology of microstructure for any designated properties.

Appendix A. Toward the simplification of (26)

$$\int_l \hat{N}_{11}\varepsilon_{11}^{0L}\,\mathrm{d}l = \int_l \hat{N}_{11}u_{10,1}\,\mathrm{d}l = -\int_l \hat{N}_{11,1}u_{10}\,\mathrm{d}l + \hat{N}_{11}u_{10}\big|_0^l, \tag{A.1}$$

$$\int_l \hat{M}_{22}\mathfrak{N}_{22}\,\mathrm{d}l = -\int_l \hat{M}_{22}u_{20,11}\,\mathrm{d}l = -\int_l \hat{M}_{22,11}u_{20}\,\mathrm{d}l + \hat{M}_{22,1}u_{20}\big|_0^l - \hat{M}_{22}u_{20,1}\big|_0^l, \tag{A.2}$$

$$\int_l \hat{M}_{33}\mathfrak{N}_{33}\,\mathrm{d}l = -\int_l \hat{M}_{33}u_{30,11}\,\mathrm{d}l = -\int_l \hat{M}_{33,11}u_{30}\,\mathrm{d}l + \hat{M}_{33,1}u_{30}\big|_0^l - \hat{M}_{33}u_{30,1}\big|_0^l, \tag{A.3}$$

$$\int_l \hat{T}\Theta\,\mathrm{d}l = \int_l \hat{T}\hat{\theta}_{,1}\,\mathrm{d}l = -\int_l \hat{T}_{,1}\hat{\theta}\,\mathrm{d}l + \hat{T}\hat{\theta}\big|_0^l. \tag{A.4}$$

Appendix B. Expressions for K_N, K_L and K_P

$$\boldsymbol{K}_N = \frac{l}{6}\sigma_1^0
\begin{bmatrix}
0 & 0 & 0 & 0 & 0 & 0 & 0 & 0 & 0 & 0 & 0 & 0 \\
 & 0 & 0 & 0 & 0 & 0 & 0 & 0 & 0 & 0 & 0 & 0 \\
 & & 0 & 0 & 0 & 0 & 0 & 0 & 0 & 0 & 0 & 0 \\
 & & & 0 & 0 & 0 & 0 & 0 & 0 & 0 & 0 & 0 \\
 & & & & 2 & 0 & 0 & 0 & 0 & 0 & 1 & 0 \\
 & & & & & 2 & 0 & 0 & 0 & 0 & 0 & 1 \\
 & & & & & & 0 & 0 & 0 & 0 & 0 & 0 \\
 & & & & & & & 0 & 0 & 0 & 0 & 0 \\
 & \text{symm.} & & & & & & & 0 & 0 & 0 & 0 \\
 & & & & & & & & & 0 & 0 & 0 \\
 & & & & & & & & & & 2 & 0 \\
 & & & & & & & & & & & 2
\end{bmatrix}. \tag{B.1}$$

To write $\boldsymbol{K}_L$ and $\boldsymbol{K}_P$ we split them into blocks:

$$\boldsymbol{K}_L = \begin{bmatrix} \boldsymbol{K}_L^{11} & \boldsymbol{K}_L^{12} \\ \boldsymbol{K}_L^{12} & \boldsymbol{K}_L^{22} \end{bmatrix}, \tag{B.2}$$

with

$$\boldsymbol{K}_L^{11} = \frac{E}{lA}
\begin{bmatrix}
A^2 & 0 & 0 & 0 & AI_3 & -AI_2 \\
 & \dfrac{12(-I_2^2+AI_{22})}{l^2} & \dfrac{12(-I_2I_3+AI_{23})}{l^2} & 0 & \dfrac{6(I_2I_3-AI_{23})}{l} & \dfrac{6(-I_2^2+AI_{22})}{l} \\
 & & \dfrac{12(-I_3^2+AI_{33})}{l^2} & 0 & \dfrac{6(I_3^2-AI_{33})}{l} & \dfrac{6(-I_2I_3+AI_{23})}{l} \\
 & & & \dfrac{A\mu I_{\mathrm{rr}}}{E} & 0 & 0 \\
 & \text{symm.} & & & (-3I_3^2+4AI_{33}) & (3I_2I_3-4AI_{23}) \\
 & & & & & (-3I_2^2+4AI_{22})
\end{bmatrix}, \tag{B.3}$$

$$\boldsymbol{K}_L^{12} = \frac{E}{lA} \begin{bmatrix} -A^2 & 0 & 0 & 0 & -AI_3 & AI_2 \\ & \dfrac{12(I_2^2 - AI_{22})}{l^2} & \dfrac{12(I_2 I_3 - AI_{23})}{l^2} & 0 & \dfrac{6(I_2 I_3 - AI_{23})}{l} & \dfrac{6(-I_2^2 + AI_{22})}{l} \\ & & \dfrac{12(I_3^2 - AI_{33})}{l^2} & 0 & \dfrac{6(I_3^2 - AI_{33})}{l} & \dfrac{6(-I_2 I_3 + AI_{23})}{l} \\ & \text{symm.} & & -\dfrac{A\mu I_{\mathrm{rr}}}{E} & 0 & 0 \\ & & & & (-3I_3^2 + 2AI_{33}) & (3I_2 I_3 - 2AI_{23}) \\ & & & & & (-3I_2^2 + 2AI_{22}) \end{bmatrix}, \qquad \text{(B.4)}$$

$$\boldsymbol{K}_L^{22} = \frac{E}{lA} \begin{bmatrix} A^2 & 0 & 0 & 0 & AI_3 & -AI_2 \\ & \dfrac{12(-I_2^2 + AI_{22})}{l^2} & \dfrac{12(-I_2 I_3 + AI_{23})}{l^2} & 0 & \dfrac{6(-I_2 I_3 + AI_{23})}{l} & \dfrac{6(I_2^2 - AI_{22})}{l} \\ & & \dfrac{12(-I_3^2 + AI_{33})}{l^2} & 0 & \dfrac{6(-I_3^2 + AI_{33})}{l} & \dfrac{6(I_2 I_3 - AI_{23})}{l} \\ & \text{symm.} & & \dfrac{A\mu I_{\mathrm{rr}}}{E} & 0 & 0 \\ & & & & (-3I_3^2 + 4AI_{33}) & (3I_2 I_3 - 4AI_{23}) \\ & & & & & (-3I_2^2 + 4AI_{22}) \end{bmatrix}. \qquad \text{(B.5)}$$

To express $\boldsymbol{K}_P$ we first define

$$\mathcal{S} = M_0 \{M_1^2 + M_2^2 + M_3^2\}^{1/2}, \qquad \text{(B.6)}$$

$$\begin{aligned}
\mathcal{D}_1 = E\Big(&-3I_3^2 (l - 2l_p)^2 M_2^2 N_0^4 - 6I_2 I_3 (l - 2l_p)^2 M_2 M_3 N_0^4 \\
& + \big(-3I_2^2 (l - 2l_p)^2 M_3^2 + 4A(l^2 - 3ll_p + 3l_p^2)(I_{33} M_2^2 + 2I_{23} M_2 M_3 + I_{22} M_3^2)\big) N_0^4 \\
& + 4AI_3 l^2 M_2 N N_0^2 \mathcal{S} + 4AI_2 l^2 M_3 N N_0^2 \mathcal{S} + 4A^2 l^2 N^2 \mathcal{S}^2 \Big) + AI_{rr} l^2 M_1^2 N_0^4 v,
\end{aligned} \qquad \text{(B.7)}$$

$$\mathcal{N}_1 = I_3 M_2 N_0^2 + I_2 M_3 N_0^2 + 2ANS, \qquad \text{(B.8)}$$

$$\mathcal{N}_2 = -AI_{23} M_2 + I_2 I_3 M_2 + I_2^2 M_3 - AI_{22} M_3, \qquad \text{(B.9)}$$

$$\mathcal{N}_3 = I_3^2 M_2 - AI_{33} M_2 - AI_{23} M_3 + I_2 I_3 M_3, \qquad \text{(B.10)}$$

$$\mathcal{N}_4 = \big(-3I_3^2 (l - 2l_p) M_2 - 3I_2 I_3 (l - 2l_p) M_3 + 2A(2l - 3l_p)(I_{33} M_2 + I_{23} M_3)\big) N_0^2 + 2AI_3 l N \mathcal{S}, \qquad \text{(B.11)}$$

$$\mathcal{N}_5 = \big(-3I_2 (l - 2l_p)(I_3 M_2 + I_2 M_3) + 2A(2l - 3l_p)(I_{23} M_2 + I_{22} M_3)\big) N_0^2 + 2AI_2 l N \mathcal{S}, \qquad \text{(B.12)}$$

$$\mathcal{N}_6 = \big(-3I_2 (l - 2l_p)(I_3 M_2 + I_2 M_3) + 2A(l - 3l_p)(I_{23} M_2 + I_{22} M_3)\big) N_0^2 - 2AI_2 l N \mathcal{S}, \qquad \text{(B.13)}$$

$$\mathcal{N}_7 = \big(3I_3^2 (l - 2l_p) M_2 + 3I_2 I_3 (l - 2l_p) M_3 - 2A(l - 3l_p)(I_{33} M_2 + I_{23} M_3)\big) N_0^2 + 2AI_3 l N \mathcal{S}. \qquad \text{(B.14)}$$

Here N_0 and M_0 are the fully plastic axial force and the fully plastic bending moment, respectively.

Then write

$$
\boldsymbol{K}_P = \begin{bmatrix}
{}^{11}\boldsymbol{K}_P^{11} & {}^{12}\boldsymbol{K}_P^{11} & {}^{11}\boldsymbol{K}_P^{12} & {}^{12}\boldsymbol{K}_P^{12} \\
 & {}^{22}\boldsymbol{K}_P^{11} & {}^{12}\boldsymbol{K}_P^{12} & {}^{22}\boldsymbol{K}_P^{12} \\
 & & {}^{11}\boldsymbol{K}_P^{22} & {}^{12}\boldsymbol{K}_P^{22} \\
\text{symm.} & & & {}^{22}\boldsymbol{K}_P^{22}
\end{bmatrix}, \tag{B.15}
$$

with

$$
{}^{11}\boldsymbol{K}_P^{11} = \frac{E(l-2l_p)}{lA\mathcal{D}_1}
\begin{bmatrix}
\dfrac{A^2 E l^2 \mathcal{N}_1^2}{(l-2l_p)} & 6AE\mathcal{N}_2 N_0^2 \mathcal{N}_1 & 6AE\mathcal{N}_3 N_0^2 \mathcal{N}_1 \\[2mm]
 & \dfrac{36E(l-2l_p)\mathcal{N}_2^2 N_0^4}{l^2} & \dfrac{36E(l-2l_p)\mathcal{N}_2\mathcal{N}_3 N_0^4}{l^2} \\[2mm]
\text{symm.} & & \dfrac{36E(l-2l_p)\mathcal{N}_3^2 N_0^4}{l^2}
\end{bmatrix}, \tag{B.16}
$$

$$
{}^{12}\boldsymbol{K}_P^{11} = \frac{E(l-2l_p)}{lA\mathcal{D}_1}
\begin{bmatrix}
\dfrac{A^2 I_{rr} l^2 M_1 N_0^2 \mathcal{N}_1 v}{(l-2l_p)} & \dfrac{AEl\mathcal{N}_1 \mathcal{N}_4}{(l-2l_p)} & -\dfrac{lAE\mathcal{N}_1 \mathcal{N}_5}{(l-2l_p)} \\[2mm]
6AI_{rr} M_1 \mathcal{N}_2 N_0^4 v & \dfrac{6E\mathcal{N}_2 N_0^2 \mathcal{N}_4}{l} & -\dfrac{6E\mathcal{N}_2 N_0^2 \mathcal{N}_5}{l} \\[2mm]
6AI_{rr} M_1 \mathcal{N}_3 N_0^4 v & \dfrac{6E\mathcal{N}_3 N_0^2 \mathcal{N}_4}{l} & -\dfrac{6E\mathcal{N}_3 N_0^2 \mathcal{N}_5}{l}
\end{bmatrix}, \tag{B.17}
$$

$$
{}^{22}\boldsymbol{K}_P^{11} = \frac{E(l-2l_p)}{lA\mathcal{D}_1}
\begin{bmatrix}
\dfrac{A^2 I_{rr}^2 l^2 M_1^2 N_0^4 v^2}{(l-2l_p)} & \dfrac{EAlI_{rr} M_1 N_0^2 \mathcal{N}_4 v}{(l-2l_p)} & -\dfrac{lAI_{rr} M_1 N_0^2 \mathcal{N}_5 v}{(l-2l_p)} \\[2mm]
 & \dfrac{E\mathcal{N}_4^2}{(l-2l_p)} & -\dfrac{E\mathcal{N}_5 \mathcal{N}_4}{(l-2l_p)} \\[2mm]
\text{symm.} & & \dfrac{E\mathcal{N}_5^2}{(l-2l_p)}
\end{bmatrix}, \tag{B.18}
$$

$$
{}^{11}\boldsymbol{K}_P^{12} =
\begin{bmatrix}
-\dfrac{Al(E\mathcal{N}_1)^2}{\mathcal{D}_1} & -\dfrac{6E^2(l-2l_p)\mathcal{N}_2 N_0^2 \mathcal{N}_1}{l\mathcal{D}_1} & -\dfrac{6E^2(l-2l_p)\mathcal{N}_3 N_0^2 \mathcal{N}_1}{l\mathcal{D}_1} \\[2mm]
 & -\dfrac{36E^2(l-2l_p)^2 \mathcal{N}_2^2 N_0^4}{Al^3 \mathcal{D}_1} & -\dfrac{36E^2(l-2l_p)^2 \mathcal{N}_3 \mathcal{N}_2 N_0^4}{Al^3 \mathcal{D}_1} \\[2mm]
\text{symm.} & & -\dfrac{36E^2(l-2l_p)^2 \mathcal{N}_3^2 N_0^4}{Al^3 \mathcal{D}_1}
\end{bmatrix}, \tag{B.19}
$$

$$
{}^{12}\boldsymbol{K}_P^{12} =
\begin{bmatrix}
-\dfrac{AEI_{rr} l M_1 N_0^2 \mathcal{N}_1 v}{\mathcal{D}_1} & -\dfrac{E^2 \mathcal{N}_1 \mathcal{N}_7}{\mathcal{D}_1} & -\dfrac{E^2 \mathcal{N}_1 \mathcal{N}_6}{\mathcal{D}_1} \\[2mm]
-\dfrac{6EI_{rr}(l-2l_p) M_1 \mathcal{N}_2 N_0^4 v}{l\mathcal{D}_1} & -\dfrac{6E^2(l-2l_p)\mathcal{N}_2 N_0^2 \mathcal{N}_7}{Al^2 \mathcal{D}_1} & -\dfrac{6E^2(l-2l_p)\mathcal{N}_2 N_0^2 \mathcal{N}_6}{Al^2 \mathcal{D}_1} \\[2mm]
-\dfrac{6EI_{rr}(l-2l_p) M_1 \mathcal{N}_3 N_0^4 v}{l\mathcal{D}_1} & -\dfrac{6E^2(l-2l_p)\mathcal{N}_3 N_0^2 \mathcal{N}_7}{Al^2 \mathcal{D}_1} & -\dfrac{6E^2(l-2l_p)\mathcal{N}_3 N_0^2 \mathcal{N}_6}{Al^2 \mathcal{D}_1}
\end{bmatrix}, \tag{B.20}
$$

$$^{22}\boldsymbol{K}_P^{12} = \begin{bmatrix} -\dfrac{AI_{rr}^2 l M_1^2 N_0^4 v^2}{\mathcal{D}_1} & -\dfrac{EI_{rr}M_1 N_0^2 \mathcal{N}_7 v}{\mathcal{D}_1} & -\dfrac{EI_{rr}M_1 N_0^2 \mathcal{N}_6 v}{\mathcal{D}_1} \\ & -\dfrac{E^2 \mathcal{N}_4 \mathcal{N}_7}{Al\mathcal{D}_1} & -\dfrac{E^2 \mathcal{N}_{10}\mathcal{N}_4}{Al\mathcal{D}_1} \\ \text{symm.} & & \dfrac{E^2 \mathcal{N}_{10}\mathcal{N}_5}{Al\mathcal{D}_1} \end{bmatrix}, \tag{B.21}$$

$$^{11}\boldsymbol{K}_P^{22} = \begin{bmatrix} \dfrac{AlE\mathcal{N}_1^2}{\mathcal{D}_1} & \dfrac{6E^2(l-2l_p)\mathcal{N}_2 N_0^2 \mathcal{N}_1}{l\mathcal{D}_1} & \dfrac{6E^2(l-2l_p)\mathcal{N}_3 N_0^2 \mathcal{N}_1}{l\mathcal{D}_1} \\ & \dfrac{36E^2(l-2l_p)^2 \mathcal{N}_2^2 N_0^4}{Al^3\mathcal{D}_1} & \dfrac{36E^2(l-2l_p)^2 \mathcal{N}_3 \mathcal{N}_2 N_0^4}{Al^3\mathcal{D}_1} \\ \text{symm.} & & \dfrac{36E^2(l-2l_p)^2 \mathcal{N}_3^2 N_0^4}{Al^3\mathcal{D}_1} \end{bmatrix}, \tag{B.22}$$

$$^{12}\boldsymbol{K}_P^{22} = \begin{bmatrix} \dfrac{AEI_{rr}l M_1 N_0^2 \mathcal{N}_1 v}{\mathcal{D}_1} & \dfrac{E^2 \mathcal{N}_1 \mathcal{N}_7}{\mathcal{D}_1} & \dfrac{E^2 \mathcal{N}_1 \mathcal{N}_6}{\mathcal{D}_1} \\ \dfrac{6EI_{rr}(l-2l_p)M_1 \mathcal{N}_2 N_0^2 v}{l\mathcal{D}_1} & \dfrac{6E^2(l-2l_p)\mathcal{N}_2 N_0^2 \mathcal{N}_7}{Al^2\mathcal{D}_1} & \dfrac{6E^2(l-2l_p)\mathcal{N}_2 N_0^2 \mathcal{N}_6}{Al^2\mathcal{D}_1} \\ \dfrac{6EI_{rr}(l-2l_p)M_1 \mathcal{N}_3 N_0^4 v}{l\mathcal{D}_1} & \dfrac{6E^2(l-2l_p)\mathcal{N}_3 N_0^2 \mathcal{N}_7}{Al^2\mathcal{D}_1} & \dfrac{6E^2(l-2l_p)\mathcal{N}_3 N_0^2 \mathcal{N}_6}{Al^2\mathcal{D}_1} \end{bmatrix}, \tag{B.23}$$

$$^{22}\boldsymbol{K}_P^{22} = \begin{bmatrix} \dfrac{AI_{rr}^2 l M_1^2 N_0^4 v^2}{\mathcal{D}_1} & \dfrac{EI_{rr}M_1 N_0^2 \mathcal{N}_7 v}{\mathcal{D}_1} & \dfrac{EI_{rr}M_1 N_0^2 \mathcal{N}_6 v}{\mathcal{D}_1} \\ & \dfrac{(E\mathcal{N}_7)^2}{Al\mathcal{D}_1} & \dfrac{E^2 \mathcal{N}_6 \mathcal{N}_7}{Al\mathcal{D}_1} \\ \text{symm.} & & \dfrac{(E\mathcal{N}_6)^2}{Al\mathcal{D}_1} \end{bmatrix}, \tag{B.24}$$

Appendix C. Transformation matrices between coordinate systems

Referring to Figure 1, $\bar{x}_i$ are the global coordinates and $\bar{e}_i$ are the corresponding orthonormal basis vectors. Similarly, $\tilde{x}_i$ and $\tilde{e}_i$ are respectively the local coordinates and the corresponding basis vectors of the undeformed state and x_i and e_i are those of the deformed state. Herein, transformation matrices relating local coordinates corresponding to the deformed and undeformed states to the global coordinates are discussed. If $^{\alpha}X_i$ denote the global coordinates of the α-th node of the element in the undeformed state, then the local orthonormal basis vectors of the undeformed state can be described with respect to those of the global coordinates as

$$\tilde{e}_1 = (\Delta \tilde{X}_1 \bar{e}_1 + \Delta \tilde{X}_2 \bar{e}_2 + \Delta \tilde{X}_3 \bar{e}_3)/\tilde{L}, \tag{C.1}$$

$$\tilde{e}_2 = (\bar{e}_3 \times \tilde{e}_1)/|\bar{e}_3 \times \tilde{e}_1|, \tag{C.2}$$

$$\tilde{e}_3 = \tilde{e}_1 \times \tilde{e}_2, \tag{C.3}$$

in which

$$\Delta \tilde{X}_i = {}^2 X_i - {}^1 X_i \quad i = 1, 2, 3, \tag{C.4}$$

$$\tilde{L} = \{(\Delta \tilde{X}_1)^2 + (\Delta \tilde{X}_2)^2 + (\Delta \tilde{X}_3)^2\}^{1/2}. \tag{C.5}$$

Thus, $\tilde{\boldsymbol{e}}_i$ and $\bar{\boldsymbol{e}}_i$ ($i = 1, 2, 3$) are related via the following equation [Simo 1985]:

$$
\begin{bmatrix} \tilde{\boldsymbol{e}}_1 \\ \tilde{\boldsymbol{e}}_2 \\ \tilde{\boldsymbol{e}}_3 \end{bmatrix} = \begin{bmatrix} \Delta\tilde{X}_1/\tilde{L} & \Delta\tilde{X}_2/\tilde{L} & \Delta\tilde{X}_3/\tilde{L} \\ -\Delta\tilde{X}_2/\tilde{S} & \Delta\tilde{X}_1/\tilde{S} & 0 \\ -\Delta\tilde{X}_1\Delta\tilde{X}_3/(\tilde{L}\tilde{S}) & -\Delta\tilde{X}_2\Delta\tilde{X}_3/(\tilde{L}\tilde{S}) & \tilde{S}/\tilde{L} \end{bmatrix} \begin{bmatrix} \bar{\boldsymbol{e}}_1 \\ \bar{\boldsymbol{e}}_2 \\ \bar{\boldsymbol{e}}_3 \end{bmatrix},
\tag{C.6}
$$

where

$$
\tilde{S} = \{(\Delta\tilde{X}_1)^2 + (\Delta\tilde{X}_2)^2\}^{1/2}.
\tag{C.7}
$$

Therefore, the matrix transforming global coordinates to the local coordinates of the undeformed state is obtained as

$$
\tilde{\mathcal{T}} = \begin{bmatrix} \Delta\tilde{X}_1/\tilde{L} & \Delta\tilde{X}_2/\tilde{L} & \Delta\tilde{X}_3/\tilde{L} \\ -\Delta\tilde{X}_2/\tilde{S} & \Delta\tilde{X}_1/\tilde{S} & 0 \\ -\Delta\tilde{X}_1\Delta\tilde{X}_3/(\tilde{L}\tilde{S}) & -\Delta\tilde{X}_2\Delta\tilde{X}_3/(\tilde{L}\tilde{S}) & \tilde{S}/\tilde{L} \end{bmatrix}.
\tag{C.8}
$$

Note that, for the case when the element is parallel to the $\bar{x}_3$-axis, the local coordinates for the undeformed state are determined by

$$
\tilde{\boldsymbol{e}}_1 = \bar{\boldsymbol{e}}_3, \quad \tilde{\boldsymbol{e}}_2 = \bar{\boldsymbol{e}}_2, \quad \tilde{\boldsymbol{e}}_3 = -\bar{\boldsymbol{e}}_1.
\tag{C.9}
$$

Similarly, the transformation matrix relating local coordinates of the deformed state to the global coordinates can be obtained. For this case, $^\alpha X_i'$ is introduced to describe the global coordinates of the α-th node of the element in the deformed state. Therefore, orthonormal basis vectors in the corotational reference coordinate system $\boldsymbol{e}_i$ can be chosen as

$$
\boldsymbol{e}_1 = (\Delta X_1\bar{\boldsymbol{e}}_1 + \Delta X_2\bar{\boldsymbol{e}}_2 + \Delta X_3\bar{\boldsymbol{e}}_3)/L,
\tag{C.10}
$$

$$
\boldsymbol{e}_2 = (\tilde{\boldsymbol{e}}_3 \times \boldsymbol{e}_1)/|\tilde{\boldsymbol{e}}_3 \times \boldsymbol{e}_1|,
\tag{C.11}
$$

$$
\boldsymbol{e}_3 = \boldsymbol{e}_1 \times \boldsymbol{e}_2,
\tag{C.12}
$$

where $\Delta X_i = {}^2X_i' - {}^1X_i'$ and $L = \{(\Delta X_1)^2 + (\Delta X_2)^2 + (\Delta X_3)^2\}^{1/2}$.

By replacing $\tilde{\boldsymbol{e}}_3$ from (C.6) into (C.11), we obtain

$$
\begin{bmatrix} \boldsymbol{e}_1 \\ \boldsymbol{e}_2 \\ \boldsymbol{e}_3 \end{bmatrix} = \begin{bmatrix} \Delta X_1/L & \Delta X_2/L & \Delta X_3/L \\ -\dfrac{\Delta\tilde{X}_2\Delta\tilde{X}_3\Delta X_3}{\tilde{L}\tilde{S}L\mathcal{L}} - \dfrac{\Delta X_2\tilde{S}}{L\tilde{L}\mathcal{L}} & \dfrac{\Delta\tilde{X}_1\Delta\tilde{X}_3\Delta X_3}{\tilde{L}\tilde{S}L\mathcal{L}} - \dfrac{\Delta X_1\tilde{S}}{L\tilde{L}\mathcal{L}} & -\dfrac{\Delta\tilde{X}_1\Delta\tilde{X}_3\Delta X_2}{\tilde{L}\tilde{S}L\mathcal{L}} + \dfrac{\Delta X_1\Delta\tilde{X}_2\Delta\tilde{X}}{L\tilde{L}\tilde{S}\mathcal{L}} \\ A_{31} & A_{32} & A_{33} \end{bmatrix} \begin{bmatrix} \bar{\boldsymbol{e}}_1 \\ \bar{\boldsymbol{e}}_2 \\ \bar{\boldsymbol{e}}_3 \end{bmatrix}
\tag{C.13}
$$

where

$$
A_{31} = \frac{\Delta\tilde{X}_1\Delta\tilde{X}_3\Delta X_1\Delta X_3}{\tilde{L}\tilde{S}L^2\mathcal{L}} + \frac{\Delta X_1^2\tilde{S}}{L^2\tilde{L}\mathcal{L}} + \frac{\Delta\tilde{X}_2\Delta\tilde{X}_3\Delta X_2\Delta X_3}{\tilde{L}\tilde{S}L^2\mathcal{L}} + \frac{\Delta X_2^2\tilde{S}}{L^2\tilde{L}\mathcal{L}},
$$

$$A_{32} = \frac{\Delta \tilde{X}_1 \Delta \tilde{X}_3 \Delta X_1 \Delta X_2}{\tilde{L} \tilde{S} L^2 \mathcal{L}} - \frac{\Delta X_1^2 \Delta \tilde{X}_2 \Delta \tilde{X}_3}{L^2 \tilde{L} \tilde{S} \mathcal{L}} - \frac{\Delta \tilde{X}_2 \Delta \tilde{X}_3 \Delta X_3^2}{\tilde{L} \tilde{S} L^2 \mathcal{L}} - \frac{\Delta X_2 \Delta X_3 \tilde{S}}{L^2 \tilde{L} \mathcal{L}},$$

$$A_{33} = \frac{\Delta \tilde{X}_1 \Delta \tilde{X}_3 \Delta X_1 \Delta X_3}{\tilde{L} \tilde{S} L^2 \mathcal{L}} + \frac{\Delta X_1^2 \tilde{S}}{L^2 \tilde{L} \mathcal{L}} + \frac{\Delta \tilde{X}_2 \Delta \tilde{X}_3 \Delta X_2 \Delta X_3}{\tilde{L} \tilde{S} L^2 \mathcal{L}} + \frac{\Delta X_2^2 \tilde{S}}{L^2 \tilde{L} \mathcal{L}},$$

$$\mathcal{L} = \left\{ \left(-\frac{\Delta \tilde{X}_2 \Delta \tilde{X}_3 \Delta X_3}{\tilde{L} \tilde{S} L} - \frac{\Delta X_2 \tilde{S}}{L \tilde{L}} \right)^2 + \left(\frac{\Delta \tilde{X}_1 \Delta \tilde{X}_3 \Delta X_3}{\tilde{L} \tilde{S} L} + \frac{\Delta X_1 \tilde{S}}{L \tilde{L}} \right)^2 \right.$$
$$\left. + \left(-\frac{\Delta \tilde{X}_1 \Delta \tilde{X}_3 \Delta X_2}{\tilde{L} \tilde{S} L} + \frac{\Delta X_1 \Delta \tilde{X}_2 \Delta \tilde{X}_3}{L \tilde{L} \tilde{S}} \right)^2 \right\}^{1/2}. \qquad \text{(C.14)}$$

Thus, the transformation matrix is obtained as

$$\mathcal{T} = \begin{bmatrix} \Delta X_1/L & \Delta X_2/L & \Delta X_3/L \\ -\frac{\Delta \tilde{X}_2 \Delta \tilde{X}_3 \Delta X_3}{\tilde{L} \tilde{S} L \mathcal{L}} - \frac{\Delta X_2 \tilde{S}}{L \tilde{L} \mathcal{L}} & \frac{\Delta \tilde{X}_1 \Delta \tilde{X}_3 \Delta X_3}{\tilde{L} \tilde{S} L \mathcal{L}} + \frac{\Delta X_1 \tilde{S}}{L \tilde{L} \mathcal{L}} & -\frac{\Delta \tilde{X}_1 \Delta \tilde{X}_3 \Delta X_2}{\tilde{L} \tilde{S} L \mathcal{L}} + \frac{\Delta X_1 \Delta \tilde{X}_2 \Delta \tilde{X}_3}{L \tilde{L} \tilde{S} \mathcal{L}} \\ B_{31} & B_{32} & B_{33} \end{bmatrix}, \qquad \text{(C.15)}$$

where

$$B_{31} = \frac{\Delta \tilde{X}_1 \Delta \tilde{X}_3 \Delta X_1 \Delta X_3}{\tilde{L} \tilde{S} L^2 \mathcal{L}} + \frac{\Delta X_1^2 \tilde{S}}{L^2 \tilde{L} \mathcal{L}} + \frac{\Delta \tilde{X}_2 \Delta \tilde{X}_3 \Delta X_2 \Delta X_3}{\tilde{L} \tilde{S} L^2 \mathcal{L}} + \frac{\Delta X_2^2 \tilde{S}}{L^2 \tilde{L} \mathcal{L}},$$

$$B_{32} = \frac{\Delta \tilde{X}_1 \Delta \tilde{X}_3 \Delta X_1 \Delta X_2}{\tilde{L} \tilde{S} L^2 \mathcal{L}} - \frac{\Delta X_1^2 \Delta \tilde{X}_2 \Delta \tilde{X}_3}{L^2 \tilde{L} \tilde{S} \mathcal{L}} - \frac{\Delta \tilde{X}_2 \Delta \tilde{X}_3 \Delta X_3^2}{\tilde{L} \tilde{S} L^2 \mathcal{L}} - \frac{\Delta X_2 \Delta X_3 \tilde{S}}{L^2 \tilde{L} \mathcal{L}},$$

$$B_{33} = \frac{\Delta \tilde{X}_1 \Delta \tilde{X}_3 \Delta X_1 \Delta X_3}{\tilde{L} \tilde{S} L^2 \mathcal{L}} + \frac{\Delta X_1^2 \tilde{S}}{L^2 \tilde{L} \mathcal{L}} + \frac{\Delta \tilde{X}_2 \Delta \tilde{X}_3 \Delta X_2 \Delta X_3}{\tilde{L} \tilde{S} L^2 \mathcal{L}} + \frac{\Delta X_2^2 \tilde{S}}{L^2 \tilde{L} \mathcal{L}}.$$

Finally, the transformation matrix for changing the generalized element coordinates consisting of 12 components in the global reference frame to the corresponding coordinates in the corotational reference frame is given by

$$\mathcal{Q} = \begin{bmatrix} \mathcal{T} & & & 0 \\ & \mathcal{T} & & \\ & & \mathcal{T} & \\ 0 & & & \mathcal{T} \end{bmatrix}. \qquad \text{(C.16)}$$

Then, components of the second-order tensors, such as the tangent stiffness matrix, as well as first-order tensors, like the generalized nodal displacements and the generalized nodal forces, are transformed to the global coordinates system based on quotient rule using the presented transformation matrices.

Appendix D.

Two of the extensively used vector homotopy functions are the fixed-point homotopy function and the Newton homotopy function, defined respectively as

$$\boldsymbol{H}_F(\boldsymbol{X}, t) = t \boldsymbol{F}(\boldsymbol{X}) + (1 - t)(\boldsymbol{X} - \boldsymbol{X}_0) = 0, \quad 0 \le t \le 1, \qquad \text{(D.1)}$$

$$\boldsymbol{H}_N(\boldsymbol{X}, t) = t\boldsymbol{F}(\boldsymbol{X}) + (1 - t)(\boldsymbol{F}(\boldsymbol{X}) - \boldsymbol{F}(\boldsymbol{X}_0)) = 0, \quad 0 \le t \le 1. \tag{D.2}$$

Here, $\boldsymbol{X}_0$ represents the initial guess of the solution. Using the vector homotopy method, the solution of $\boldsymbol{F}(\boldsymbol{X}) = 0$ can be obtained by numerically integrating the following relation:

$$\dot{\boldsymbol{X}} = -\left(\frac{\partial \boldsymbol{H}}{\partial \boldsymbol{X}}\right)^{-1} \frac{\partial \boldsymbol{H}}{\partial t}, \quad 0 \le t \le 1, \tag{D.3}$$

which requires the inversion of the matrix $\partial \boldsymbol{H}/\partial \boldsymbol{X}$ at each iteration.

A series of iterative Newton homotopy methods has also been developed, where $Q(t)$ does not need to be determined [Dai et al. 2014]. Considering $\dot{\boldsymbol{X}} = \lambda \boldsymbol{u}$, the general form of the scalar Newton homotopy function becomes

$$\dot{\boldsymbol{X}} = -\frac{\dot{Q}(t)}{2Q(t)} \frac{\|\boldsymbol{F}(\boldsymbol{X})\|^2}{\boldsymbol{F}^T \boldsymbol{B}\boldsymbol{u}} \boldsymbol{u}. \tag{D.4}$$

Using the forward Euler method, (D.4) is discretized and the general form of the iterative Newton homotopy method is obtained as

$$X(t + \Delta t) = X(t) - (1 - \gamma) \frac{\boldsymbol{F}^T \boldsymbol{B}\boldsymbol{u}}{\|\boldsymbol{B}\boldsymbol{u}\|^2} \boldsymbol{u}, \tag{D.5}$$

where $-1 < \gamma < 1$.

The reason homotopy methods converge with the required accuracy in the case of complex problems (in the presence of the plasticity and buckling in a large number of members of the microlattice) is thanks to raising the position of the driving vector $\boldsymbol{u}$ in $\dot{\boldsymbol{X}} = \lambda \boldsymbol{u}$ to introduce the best descent direction in searching the solution vector $\boldsymbol{X}$. In the so-called continuous Newton method we have $\boldsymbol{u} = \boldsymbol{B}^{-1}\boldsymbol{F}$, resulting in loss of accuracy from inverting the Jacobian matrix when it is singular or severely ill-conditioned, leading to oscillatory, nonconvergent behavior. Whereas in (76), we have $\boldsymbol{u} = \boldsymbol{B}^T \boldsymbol{F}$ with $\lambda = -\frac{1}{2}\dot{Q}\|\boldsymbol{F}\|^2/(Q\|\boldsymbol{B}^T\boldsymbol{F}\|^2)$, and it can also be expressed by two vectors such as $\boldsymbol{F}$ and $\boldsymbol{B}^T\boldsymbol{F}$. The hypersurface formulated in (75) defines a future cone in the Minkowski space $\mathbb{M}^{n+1}$ in terms of the residual vector $\boldsymbol{F}$ and a positive and monotonically increasing function $Q(t)$ as

$$\mathcal{X}^T \boldsymbol{g} \mathcal{X} = 0, \tag{D.6}$$

where

$$\mathcal{X} = \begin{bmatrix} \boldsymbol{F}(\boldsymbol{X})/\|\boldsymbol{F}(\boldsymbol{X}_0)\| \\ 1/\sqrt{Q(t)} \end{bmatrix}, \tag{D.7}$$

$$\boldsymbol{g} = \begin{bmatrix} \boldsymbol{I}_n & \boldsymbol{0}_{n \times 1} \\ \boldsymbol{0}_{1 \times n} & -1 \end{bmatrix}, \tag{D.8}$$

and $\boldsymbol{I}_n$ is the $n \times n$ identity matrix. Then the solution vector $\boldsymbol{X}$ is searched along the path kept on the manifold defined by the following equation:

$$\|\boldsymbol{F}(\boldsymbol{X})\|^2 = \frac{\|\boldsymbol{F}(\boldsymbol{X}_0)\|^2}{Q(t)}. \tag{D.9}$$

Therefore, an absolutely convergent property is achieved by guaranteeing $Q(t)$ as a monotonically increasing function of t. In fact, (D.9) enforces the residual error $\|\boldsymbol{F}(\boldsymbol{X})\|$ to vanish when t is large.

References

[Ashby et al. 2000] M. F. Ashby, A. G. Evans, N. A. Fleck, L. J. Gibson, J. W. Hutchinson, and H. N. G. Wadley, *Metal foams: a design guide*, Butterworth-Heinemann, Waltham, MA, 2000.

[Bathe and Bolourchi 1979] K.-J. Bathe and S. Bolourchi, "Large displacement analysis of three-dimensional beam structures", *Int. J. Numer. Methods Eng.* **14**:7 (1979), 961–986.

[Besseling 1986] J. F. Besseling, "Large rotations in problems of structural mechanics", pp. 25–39 in *Finite element methods for nonlinear problems* (Trondheim, Norway, 1985), edited by P. G. Bergan et al., Springer, 1986.

[Cai et al. 2009a] Y. Cai, J. K. Paik, and S. N. Atluri, "Large deformation analyses of space-frame structures, using explicit tangent stiffness matrices, based on the Reissner variational principle and a von Karman type nonlinear theory in rotated reference frames", *Comput. Model. Eng. Sci.* **54**:3 (2009), 335–368.

[Cai et al. 2009b] Y. Cai, J. K. Paik, and S. N. Atluri, "Large deformation analyses of space-frame structures, with members of arbitrary cross-section, using explicit tangent stiffness matrices, based on a von Karman type nonlinear theory in rotated reference frames", *Comput. Model. Eng. Sci.* **53**:2 (2009), 117–145.

[Dai et al. 2014] H. Dai, X. Yue, and S. N. Atluri, "Solutions of the von Kármán plate equations by a Galerkin method, without inverting the tangent stiffness matrix", *J. Mech. Mater. Struct.* **9**:2 (2014), 195–226.

[Davidenko 1953] D. F. Davidenko, "On a new method of numerical solution of systems of nonlinear equations", *Dokl. Akad. Nauk SSSR* **88** (1953), 601–602. In Russian.

[Evans et al. 2010] A. G. Evans, M. Y. He, V. S. Deshpande, J. W. Hutchinson, A. J. Jacobsen, and W. Carter, "Concepts for enhanced energy absorption using hollow micro-lattices", *Int. J. Impact Eng.* **37**:9 (2010), 947–959.

[Geradin and Cardona 1988] M. Geradin and A. Cardona, "Kinematics and dynamics of rigid and flexible mechanisms using finite elements and quaternion algebra", *Comput. Mech.* **4**:2 (1988), 115–135.

[Gibson and Ashby 1988] L. J. Gibson and M. F. Ashby, *Cellular solids: structure and properties*, Pergamon, Oxford, 1988.

[Han and Gouma 2006] D. Han and P.-I. Gouma, "Electrospun bioscaffolds that mimic the topology of extracellular matrix", *Nanomedicine* **2**:1 (2006), 37–41.

[Hodge 1959] P. G. Hodge, Jr., *Plastic analysis of structures*, McGraw-Hill, New York, 1959.

[Hutmacher 2000] D. W. Hutmacher, "Scaffolds in tissue engineering bone and cartilage", *Biomater.* **21**:24 (2000), 2529–2543.

[Izzuddin 2001] B. A. Izzuddin, "Conceptual issues in geometrically nonlinear analysis of 3D framed structures", *Comput. Methods Appl. Mech. Eng.* **191**:8-10 (2001), 1029–1053.

[Kondoh and Atluri 1987] K. Kondoh and S. N. Atluri, "Large-deformation, elasto-plastic analysis of frames under nonconservative loading, using explicitly derived tangent stiffnesses based on assumed stresses", *Comput. Mech.* **2**:1 (1987), 1–25.

[Kondoh et al. 1986] K. Kondoh, K. Tanaka, and S. N. Atluri, "An explicit expression for tangent-stiffness of a finitely deformed 3-D beam and its use in the analysis of space frames", *Comput. Struct.* **24**:2 (1986), 253–271.

[Liu et al. 2009] C.-S. Liu, W. Yeih, C.-L. Kuo, and S. N. Atluri, "A scalar homotopy method for solving an over/under-determined system of non-linear algebraic equations", *Comput. Model. Eng. Sci.* **53**:1 (2009), 47–71.

[Lo 1992] S. H. Lo, "Geometrically nonlinear formulation of 3D finite strain beamelement with large rotations", *Comput. Struct.* **44**:1-2 (1992), 147–157.

[Lu et al. 2005] T. J. Lu, L. Valdevit, and A. G. Evans, "Active cooling by metallic sandwich structures with periodic cores", *Prog. Mater. Sci.* **50**:7 (2005), 789–815.

[Mallett and Berke 1966] R. H. Mallett and L. Berke, "Automated method for the large deflection and instability analysis of three-dimensional truss and frame assemblies", technical report AFFDL-TR-66-102, Air Force Flight Dynamics Lab., 1966.

[Mota et al. 2015] C. Mota, D. Puppi, F. Chiellini, and E. Chiellini, "Additive manufacturing techniques for the production of tissue engineering", *J. Tissue Eng. Regener. Med.* **9**:3 (2015), 174–190.

[Punch and Atluri 1984] E. F. Punch and S. N. Atluri, "Development and testing of stable, invariant, isoparametric curvilinear 2- and 3-D hybrid-stress elements", *Comput. Methods Appl. Mech. Eng.* **47**:3 (1984), 331–356.

[Reissner 1953] E. Reissner, "On a variational theorem for finite elastic deformations", *J. Math. Phys.* **32**:1-4 (1953), 129–135.

[Salari-Sharif and Valdevit 2014] L. Salari-Sharif and L. Valdevit, "Accurate stiffness measurement of ultralight hollow metallic microlattices by laser vibrometry", *Exp. Mech.* **54**:8 (2014), 1491–1495.

[Schaedler and Carter 2016] T. A. Schaedler and W. B. Carter, "Architected cellular materials", *Annu. Rev. Mater. Res.* **46** (2016), 187–210.

[Schaedler et al. 2011] T. A. Schaedler, A. J. Jacobsen, A. Torrents, A. E. Sorensen, J. Lian, J. R. Greer, L. Valdevit, and W. B. Carter, "Ultralight metallic microlattices", *Science* **334**:6058 (2011), 962–965.

[Schaedler et al. 2014] T. A. Schaedler, C. J. Ro, A. E. Sorensen, Z. Eckel, S. S. Yang, W. B. Carter, and A. J. Jacobsen, "Designing metallic microlattices for energy absorber applications", *Adv. Eng. Mater.* **16**:3 (2014), 276–283.

[Shi and Atluri 1988] G. Shi and S. N. Atluri, "Elasto-plastic large deformation analysis of space-frames: a plastic-hinge and stress-based explicit derivation of tangent stiffnesses", *Int. J. Numer. Methods Eng.* **26**:3 (1988), 589–615.

[Simo 1985] J. C. Simo, "A finite strain beam formulation: the three-dimensional dynamic problem, I", *Comput. Methods Appl. Mech. Eng.* **49**:1 (1985), 55–70.

[Torrents et al. 2012] A. Torrents, T. A. Schaedler, A. J. Jacobsen, W. B. Carter, and L. Valdevit, "Characterization of nickel-based microlattice materials with structural hierarchy from the nanometer to the millimeter scale", *Acta Mater.* **60**:8 (2012), 3511–3523.

[Ueda and Yao 1982] Y. Ueda and T. Yao, "The plastic node method: a new method of plastic analysis", *Comput. Methods Appl. Mech. Eng.* **34**:1-3 (1982), 1089–1104.

[Ueda et al. 1968] Y. Ueda, M. Matsuishi, T. Yamakawa, and Y. Akamatsu, "Elastic-plastic analysis of framed structures using the matrix method", *J. Soc. Naval Arch. Japan* **1968**:124 (1968), 183–191. In Japanese.

[Valdevit et al. 2011] L. Valdevit, A. J. Jacobsen, J. R. Greer, and W. B. Carter, "Protocol for the optimal design of multifunctional structures: from hypersonics to micro-architected materials", *J. Am. Ceram. Soc.* **94**:s1 (2011), S15–S34.

[Valentin et al. 2006] J. E. Valentin, J. S. Badylak, G. P. McCabe, and S. F. Badylak, "Extracellular matrix bioscaffolds for orthopaedic applications: a comparative histologic study", *J. Bone Jt. Surg. Am.* **88**:12 (2006), 2673–2686.

[Wadley 2002] H. N. G. Wadley, "Cellular metals manufacturing", *Adv. Eng. Mater.* **4**:10 (2002), 726–733.

[Williams 1964] F. W. Williams, "An approach to the nonlinear behaviour of the members of a rigid jointed plane framework with finite deflections", *Quart. J. Mech. Appl. Math.* **17** (1964), 451–469.

MARYAM TABATABAEI: maryam.tabatabaei@ttu.edu
Center for Advanced Research in the Engineering Sciences, Institute for Materials, Manufacturing, and Sustainment, Texas Tech University, Lubbock, TX, United States

DY LE: dy.d.le@ttu.edu
Center for Advanced Research in the Engineering Sciences, Institute for Materials, Manufacturing, and Sustainment, Texas Tech University, Lubbock, TX, United States

SATYA N. ATLURI: snatluri.ttu@gmail.com
Center for Advanced Research in the Engineering Sciences, Institute for Materials, Manufacturing, and Sustainment, Texas Tech University, Lubbock, TX, United States

Cover photo: Wikimedia Commons

Journal of Mechanics of Materials and Structures